Tbr1 autism mouse model displays altered structural and functional amygdalar connectivity and abnormal whole-brain synchronization

Tsan-Ting Hsu[1], Chien-Yao Wang[2] and Yi-Ping Hsueh[1]*

[1]Institute of Molecular Biology, Academia Sinica, Taipei, Taiwan, ROC
[2]Institute of Information Science, Academia Sinica, Taipei, Taiwan, ROC

* Corresponding to Dr. Yi-Ping Hsueh, Institute of Molecular Biology, Academia Sinica, 128, Sec 2, Academia Rd, Taipei, 11529, Taiwan, ROC. Email: yph@gate.sinica.edu.tw

Running title: Whole-brain connectivity in *Tbr1*$^{+/-}$ autism model.

Keywords: Axonal projection, Contralateral long-range connectivity, Autism spectrum disorders, Basolateral amygdala, Default mode network, Structural and functional connectivity, Whole-brain connectivity.

Abstract

Autism spectrum disorders (ASD) are recognized as neural disconnectivity syndromes. Here, we establish a whole-brain immunostaining and quantification platform to investigate structural and functional connectivity in a *Tbr1*$^{+/-}$ autism mouse model, which shares a defect in the anterior commissure that is evolutionarily conserved with human patients. Since the basolateral amygdala (BLA) is particularly susceptible to *Tbr1* haploinsufficiency and it projects to the contralateral brain hemisphere via the anterior commissure, we express a channelrhodopsin variant oChIEF fused with Citrine at the BLA to outline axonal projections of BLA neurons and to activate the BLA under blue light theta-burst stimulation (TBS). Next, we evaluate C-FOS expression to represent neural activity. We show that *Tbr1* haploinsufficiency almost completely disrupts contralateral BLA axonal projections and results in ipsilateral mistargeting, thereby globally altering BLA functional connectivity. Based on correlated C-FOS expression among brain regions, we further report that *Tbr1* deficiency severely disrupts whole-brain synchronization in the absence of salient stimulation. *Tbr1*$^{+/-}$ and wild-type mice exhibit opposing responses to TBS-induced amygdalar activation, with it reducing synchronization in wild-type mice but enhancing it in *Tbr1*$^{+/-}$ mice. Whole-brain modular organization and inter-module connectivity are also affected by Tbr1 deficiency and amygdalar activation. In fact, the synchronization and intra- and inter-modular connectivities of TBS-treated *Tbr1*$^{+/-}$ mice are more comparable to those of non-treated wild-type mice, suggesting a potential ameliorating effect of amygdalar stimulation on brain function. Moreover, *Tbr1*$^{+/-}$ mice exhibit attenuated connectivity between the amygdala and default mode network, a subnetwork highly relevant to social behaviors, strengthening the link between the impaired connectivity and social behavior deficits displayed by *Tbr1*$^{+/-}$ mice. Our high-resolution analytical platform reveals the inter- and intra-hemispheric connectopathies arising from an ASD condition and emphasizes the defective synchronization at a whole-brain scale caused by *Tbr1* deficiency.

Introduction

Autism spectrum disorders (ASD), one of the most highly prevalent neurodevelopmental disorders, are characterized by two core behavioral deficits that appear in early childhood; one is impaired social interaction and communication, and the other is restricted, repetitive behavioral patterns and sensory abnormalities (https://dsm.psychiatryonline.org/doi/book/10.1176/appi.books.9780890425787). Seeking the biological mechanisms causing these core behavioral manifestations is crucial for providing a better understanding of ASD and uncovering potential treatments. One of the primary biological features correlated with behavioral phenotypes in ASD patients is altered brain connectivity [1-4], although the detailed features of rewiring alterations under ASD conditions remain elusive.

T-Brain-1 (TBR1), a neuron-specific T-box transcription factor [5], has been identified as a causative gene of ASD (Gene score 1, https://gene.sfari.org/database/human-gene/TBR1) [6, 7]. TBR1 regulates the expression of a set of genes controlling axonal projections of cortical and amygdalar neurons [7, 8]. Contralateral projection of basolateral amygdalae (BLA) neurons via the posterior part of the anterior commissure is particularly sensitive to *Tbr1* deficiency [7], with this latter eliciting anterior commissure impairment in both humans and mice [7, 9-11]. Moreover, *Tbr1* haploinsufficiency, a condition mimicking genetic variations observed in patients with ASD, results in many autism-like behavioral abnormalities in mice, including reduced social behaviors, defective vocalization, impaired olfactory discrimination, aversive memory and cognitive inflexibility [7, 8, 12]. Disconnection of the anterior commissure in mice either surgically or via unilateral chemogenetic inhibition of the BLA results in autism-like behaviors [13, 14]. Together, these studies have demonstrated that *Tbr1*$^{+/-}$ mice may serve as an excellent model for exploring the connectivity deficits associated with ASD.

Given that BLA axonal projection is particularly sensitive to *Tbr1* haploinsufficiency [7, 13] and that BLA activation by local infusion of D-cycloserine, a co-agonist of NMDAR, is sufficient to ameliorate the autism-like behaviors exhibited by *Tbr1*$^{+/-}$ mice [7], we speculate that BLA-derived circuits are critical to *TBR1*-linked ASD phenotypes. Here, we established a whole-brain analytical platform using serial mouse brain sections for immunostaining and high-content imaging and for performing registration and quantification based on the Allen Mouse Common Coordinate Framework version 3 (CCFv3) [15]. Using this system, we analyzed axonal projection of the BLA at the mesoscale level and assessed neuronal activity based on C-FOS expression at a cellular level. Our high-resolution analyses revealed the inter- and intra-hemispheric connectopathy in *Tbr1*$^{+/-}$ mice, providing clear evidence that an ASD-linked condition results in dyssynchronization at the whole-brain scale.

80

81 **Results**

82 **Development of a mesoscopic whole-brain scale circuit analysis pipeline**

83 To analyze structural and functional BLA connectivity in individual mice, we unilaterally
84 expressed the ultra-fast channelrhodopsin variant oChIEF fused with the fluorescent protein
85 Citrine in BLA neurons of both *Tbr1*$^{+/-}$ and wild-type mice. Given that oChIEF-Citrine targets
86 the plasma membrane of entire neurons, in addition to opto-stimulating BLA neurons, oChIEF-
87 Citrine was also used to outline BLA neurons, including axons. The relative fluorescent signal
88 intensity of oChIEF-Critine outside of the BLA reflects the extent of axonal projections derived
89 from unilateral BLA neurons. To analyze neuronal activity and functional connectivity of the
90 BLA, *Tbr1*$^{+/-}$ and wild-type mice were further separated into two groups. One group received
91 optical theta-burst stimulation (TBS) at the oChIEF-expressing BLA when they were freely
92 moving in their home cages. The other control group was subjected to the same experimental
93 procedure except for optical stimulation. Then, we analyzed neuronal activation by BLA
94 stimulation based on C-FOS expression 2 hr after stimulation. Our whole-brain scale analysis
95 and quantification basically comprise five elements, with an outline and detailed procedure
96 being presented in **Figures 1, S1** and the **Methods**. The list of brain regions used in our study
97 and their corresponding abbreviations can be found in **Tables S1** and **S2**. Brain ontology is
98 identical to CCFv3.

99

100 **Structure-wise comparisons reveal rewiring in *Tbr1*$^{+/-}$ mouse brains**

101 First, we analyzed the whole-brain distribution pattern of oChIEF-Citrine. We found that
102 oChIEF-Citrine signals were widely distributed ipsilaterally in wild-type brains and also
103 extended contralaterally (**Figure 2A**; **Video S1**, upper). However, oChIEF-Citrine signals
104 barely extended contralaterally in *Tbr1*$^{+/-}$ mouse brains (**Figure 2a**; **Video S1**, lower).

105 We compared brains from a total of 15 *Tbr1*$^{+/-}$ mice and 13 wild-type littermates. Since
106 the BLA consists of heterologous projections with varying patterns of long-range axonal
107 projection [16], first we investigated the distributions of the virus injection sites between wild-
108 type and *Tbr1*$^{+/-}$ mouse brains and confirmed that they were indistinguishable and comparable
109 (**Figure S2**). Next, we binned and summarized the average percentage of oChIEF-Citrine
110 signals in all brain regions of *Tbr1*$^{+/-}$ mice and wild-type littermates. These results were
111 subjected to 3D projection at both coronal and horizontal views, which indicated a reduction in
112 contralateral projections of BLA neurons in *Tbr1*$^{+/-}$ mice (**Figure 2B**; **Video S2**).

113 Moreover, we used three different methods to identify brain regions susceptible to *Tbr1*
114 deficiency. The first method was a structure-wise comparison between *Tbr1*$^{+/-}$ mice and wild-
115 type littermates at the whole-brain scale. This volume-based quantification was performed on
116 the ipsilateral, i.e., the virus injection site, and contralateral hemispheres separately (**Figure**
117 **S3A, Table S1**). Consistent with our previous findings [7, 13], we found that oChIEF-Citrine
118 signals were greatly reduced in contralateral BLA-related regions (LA, BLA, BLAa, BLAp),
119 and in the associated fiber tracts (act, amc), of *Tbr1*$^{+/-}$ mice compared to those of wild-type
120 littermates (**Figures 2C-2E**), supporting the reliability of our whole-brain analysis system.
121 In addition to the amygdala and its associated fiber tracts, we found that additional 26
122 brain regions at the contralateral site had much lower oChIEF-Citrine signals in *Tbr1*$^{+/-}$ mice
123 relative to wild- type (**Figures 2C-2E**). We term these regions "affected contralateral projection
124 regions (ACPR)", which mainly reside in areas of the forebrain, such as the isocortex, olfactory
125 area (OLF), cortical subplate (CTXsp) and cerebral nuclei (CNU). In wild-type mice, these
126 regions actually receive topographically bilateral projections from the two amygdalae in the
127 two brain hemispheres (**Figures 2A-2B,** upper panel; also see Allen Mouse Brain Connectivity
128 Atlas: connectivity.brain-map.org/projection/experiment/113144533 and
129 connectivity.brain.map.org/projection/experiment/277710753). At the ipsilateral site, 18 brain
130 regions were identified as exhibiting increased oChIEF-Citrine signals in *Tbr1*$^{+/-}$ mouse brains
131 (**Figures 2C-2E**), which we denote "affected ipsilateral projection regions (AIPR)". Note that
132 these AIPR are not the counterparts of the ACPR (**Figures 2C-2E**). These findings indicate that
133 *Tbr1* haploinsufficiency impairs the contralateral projections of BLA neurons and leads to
134 mistargeting to ipsilateral brain regions, and not necessarily limited to ACPR counterparts. We
135 also noticed that AIPR encompass several regions in the cortex, thalamus (TH), hypothalamus
136 (HY) and midbrain (MB) (**Figures 2C-2E**), implying that *Tbr1* haploinsufficiency may elicit
137 stronger BLA ipsilateral connections with those regions.
138 We selected 44 contralateral and 50 ipsilateral brain regions to manually verify the
139 regions of interest (ROI) and to correct mismatched ROI for every single brain slice image of
140 each brain sample, confirming our quantification results (**Figure 2E**, the regions labeled with
141 red font).
142
143 ***Tbr1* deficiency alters the ratio of contralateral to ipsilateral projections**
144 The second method we applied was to measure the ratio of Citrine signals in paired regions of
145 the two brain hemispheres, i.e., the contralateral/ipsilateral (C/I) ratio, in individual mice. The
146 fold-change in C/I ratios between *Tbr1*$^{+/-}$ mice and WT littermates were then analyzed, which

147 revealed that *Tbr1*$^{+/-}$ mice exhibited reduced C/I ratios in all identified regions (**Figure S3B**).
148 Given that all ACPR exhibited reduced Citrine signals, their C/I ratios were consequently
149 reduced (**Figure S3C**). In addition, three AIPR presented lower C/I ratios because of their
150 stronger Citrine signals at the ipsilateral site (**Figure S3D**). Moreover, 11 additional brain
151 regions in *Tbr1*$^{+/-}$ mice exhibited a reduced C/I ratio due to differential expression of the Citrine
152 levels between the two brain hemispheres (**Figure S3E**). This analysis of C/I ratios further
153 confirms the altered bilateral axonal projections elicited by *Tbr1* deficiency.
154
155 **Principal component analysis also reveals altered rewiring in *Tbr1*$^{+/-}$ mouse brains**
156 The third method was to analyze BLA projections using principal component analysis (PCA).
157 For the contralateral site, the PCA analysis showed clear segregation between wild-type and
158 *Tbr1*$^{+/-}$ mice along PC2 (**Figures S4A-S4B**; PC2 KNN classification accuracy 86%, k = 4, P =
159 0) with the ACPR identified in **Fig. 1** contributing noticeably to that axis. In fact, the top 10%
160 of regions contributing to PC2 were all ACPR (**Figures S4C-S4D**). At the ipsilateral site,
161 although our PCA analysis revealed strong and significant segregation between the two
162 genotypes along PC1 (**Figures S4E-S4F**; PC1 KNN classification accuracy 75%, k = 5, P =
163 0.013), there were no correlations between PC1 loading and AIPR (**Figures S4G-S4H**),
164 implying that many BLA ipsilateral targeting regions exhibit greater inter-sample variation than
165 the difference between genotypes and supporting that some ipsilateral projections tend to be
166 random and that their innervations are less specific.
167 Taken together, using multiple different comparative approaches, we analyzed BLA-
168 derived circuits in *Tbr1*$^{+/-}$ mice at a whole-brain scale and uncovered aberrant rewiring caused
169 by *Tbr1* haploinsufficiency. The imbalanced topographic BLA bilateral axonal projections
170 account for the major rewiring differences, with some enhanced BLA ipsilateral projections to
171 some areas of the cortex, thalamus, hypothalamus and midbrain also being displayed by the
172 *Tbr1*$^{+/-}$ mice.
173
174 ***Tbr1* deficiency changes neuronal activation**
175 Next, we investigated if the altered BLA projections in *Tbr1*$^{+/-}$ mice influence their neuronal
176 activity patterns. To do so, we compared the C-FOS expression of ACPR and AIPR across four
177 experimental groups, i.e., WT ctrl, *Tbr1*$^{+/-}$ ctrl, WT TBS and *Tbr1*$^{+/-}$ TBS. Using volume-based
178 quantification, the C-FOS expression patterns in all examined brain regions were
179 indistinguishable among the four groups (**Figure S5A**, **Table S1**). However, when we
180 visualized the distribution of C-FOS^{+} cells after binning and averaging of a 3D mouse brain

181 map, it was clear that the distribution of C-FOS$^+$ cells varied among these four groups of mice
182 (**Figure S5B**). Since a given brain region usually makes specific connections with multiple
183 brain regions via specific subregions, the unchanged subregions may dilute any differences and
184 result in indistinguishable C-FOS expression levels in a volume-based quantification. Therefore,
185 we established slice-based quantification to analyze the numbers of C-FOS$^+$ cells along the
186 anterior-posterior (AP) axis with 100 μm binning of both brain hemispheres (**Figure 3A;**
187 **Figure S6A**), which revealed differential neuronal activation between *Tbr1*$^{+/–}$ mice and wild-
188 type littermates (**Figure S6B**). Cumulative probability distributions indicated that the majority
189 of brain regions indeed displayed comparable numbers of C-FOS$^+$ cells among the four
190 experimental groups for both brain hemispheres (**Figures 3A, 3B**). However, compared to wild-
191 type groups, *Tbr1*$^{+/–}$ mice had more C-FOS$^+$ cells in a small proportion (~15%) of regions at
192 the contralateral site with or without TBS treatment (**Figure 3B**, upper). At the ipsilateral site,
193 only the WT ctrl group had fewer C-FOS$^+$ cells than the other three groups (**Figure 3B**, lower).
194 Thus, although only a few differentially activated brain regions exist, our slice-based
195 quantification approach adequately identified those regions among our experimental groups.
196 Consequently, we used this slice-based quantification approach to conduct pairwise
197 comparisons of our four experimental groups of mice to establish which brain regions exhibited
198 differential C-FOS expression (**Figure 3C**, **Table S2**). For the comparison of *Tbr1*$^{+/–}$ ctrl vs.
199 WT ctrl, we uncovered 105 and 93 regions having more C-FOS$^+$ cells in the contralateral and
200 ipsilateral sides of the brains of the *Tbr1*$^{+/–}$ ctrl group, respectively. In contrast, only 9 regions
201 displayed more C-FOS$^+$ cells in the WT ctrl (4 in the contralateral and 5 in the ipsilateral
202 hemispheres) (**Figure 3C**, left). These differentially activated regions are widely distributed
203 across the brain, from the isocortex to MB, suggesting that the abnormally high brain activities
204 of *Tbr1*$^{+/–}$ mice during wakefulness (the state of our mice under experimental/control treatment)
205 can be linked to circuits and areas distributed across the entire brain (**Figure 3C**, left).
206 We also analyzed the contributions of BLA activation to *Tbr1* phenotypes. In wild-type
207 mice, TBS at the BLA increased the number of C-FOS$^+$ cells across different brain regions of
208 both the contralateral and ipsilateral sites (**Figure 3C**, middle left). Thus, unilateral activation
209 of the BLA in wild-type mice indeed activates many other brain regions, both contralaterally
210 and ipsilaterally. In contrast, *Tbr1*$^{+/–}$ mice unexpectedly displayed more brain regions with
211 fewer C-FOS$^+$ cells upon TBS (**Figure 3C**, middle right). These results indicate that *Tbr1*
212 haploinsufficiency alters global functional connectivity between the BLA and other brain
213 regions. We also detected differing C-FOS$^+$ cell distributions in many brain regions between

214 the *Tbr1*$^{+/-}$ TBS and WT TBS groups (**Figure 3C**, right). Taken together, these results imply
215 that *Tbr1* deficiency induces functional rewiring.
216
217 **Correlations between rewired BLA-derived circuits and altered C-FOS expression**
218 **patterns**
219 To further explore the correlation between axonal projection and neural activation, we
220 conducted slice-based quantification of oChIEF-Citrine signals as per our analysis of C-FOS^{+}
221 cell distribution patterns. Compared to our volume-based quantification results, we found that
222 more brain structures exhibited differential innervation patterns of BLA-derived axons in
223 *Tbr1*$^{+/-}$ mice according to slice-based analysis, regardless of contralateral or ipsilateral
224 projection and increased or decreased innervation patterns (**Figures S7A-S7C, Table S2**).
225 However, the general conclusion of BLA-derived circuit rewiring in *Tbr1*$^{+/-}$ mice remains, i.e.,
226 that impaired contralateral axonal projections and enhanced axonal innervations in the
227 ipsilateral hemisphere.
228 Next, we selected the brain regions exhibiting rewired axonal innervations and altered
229 C-FOS expression patterns upon TBS of the BLA in either wild-type or *Tbr1*$^{+/-}$ mice for
230 correlation analysis. First, we determined ΔoChIEF traces by pairwise subtraction of oChIEF-
231 Citrine signals between *Tbr1*$^{+/-}$ and wild-type samples (**Figures 4A**, **4C,** left, 10μm^3 binning
232 cubes). Neural activation induced by TBS in *Tbr1*$^{+/-}$ mice and WT littermates, i.e., *Tbr1*$^{+/-}$ ΔC-
233 FOS traces and WT ΔC-FOS traces respectively, was also determined. Pairwise subtraction
234 between *Tbr1*$^{+/-}$ ΔC-FOS and WT ΔC-FOS traces was then executed to obtain all possible
235 differences, i.e., ΔΔC-FOS traces (**Figures 4A**, **4C,** middle, 100 μm^3 binning cubes). A Pearson
236 correlation coefficient (r) was calculated according to the correlation of the averaged ΔoChIEF
237 trace and the averaged ΔΔC-FOS trace in each brain region. The brain regions exhibiting
238 positive correlations between rewired BLA-derived circuits and altered C-FOS expression
239 patterns reflect concurrent changes to BLA-derived axonal innervations and their neural activity
240 upon BLA activation. In the contralateral hemisphere of *Tbr1*$^{+/-}$ mice, the AUD regions (AUD,
241 AUDp), AIp, PIR, BLA and MBsen regions all exhibited impaired BLA contralateral axonal
242 projections and the boosting effects of BLA activation on C-FOS expression were inhibited,
243 indicating a loss of intensification effect of contralateral BLA axonal projections to these
244 regions in the mutant mice (**Figures 4A-4B**). The contralateral thalamus, DORsm regions
245 (DORsm, VENT) and ILM each displayed higher oChIEF-Citrine signals in *Tbr1*$^{+/-}$ mice, but
246 they exhibited negative correlations between ΔoChIEF and ΔΔC-FOS (**Figures 4A-4B**).

247 In the ipsilateral hemisphere, the correlation results between ΔoChIEF and ΔΔC-FOS
248 were the opposite of those for the contralateral hemisphere (**Figures 4A-4B** vs. **Figures 4C-**
249 **4D**). Only for the posterior part (ventral) of the HIP and NOT were ipsilateral BLA axonal
250 projections reduced in *Tbr1*$^{+/-}$ mice, and it exhibited impaired boosting effects of BLA
251 activation on C-FOS expression (**Figures 4C-4D, left panel**). A major group of regions at the
252 ipsilateral side exhibited a higher level of oChIEF-Citrine in *Tbr1*$^{+/-}$ mice but a negative
253 correlation between ΔoChIEF and ΔΔC-FOS (**Figures 4C-4D**). This group contains the
254 isocortical area (MOp, AUDd, ACA, ACAv, TEa), as well as the CNU (MEA, PALv, SI, PALc,
255 BST), TH (DORsm, DORpm, CL), HY (LZ) and MB (SCdg, VTA) areas.
256 Taken together, these findings indicate that structural rewiring of BLA-derived circuits
257 in *Tbr1*$^{+/-}$ mice triggers altered functional consequences for downstream targets. In general,
258 more contralateral target areas receive fewer BLA axonal projections that cause diminished
259 potentiation of neuronal activities, whereas more ipsilateral downstream target regions are
260 innervated by more BLA axons that induce net inhibitory effects on neuronal activities.
261
262 **Altered functional connectivity of *Tbr1*$^{+/-}$ mice**
263 In addition to examining the alterations to individual structures elicited by *Tbr1*
264 haploinsufficiency, we further assessed the functional changes at the network level. We
265 evaluated the functional connectivity of paired brain regions by determining their correlated C-
266 FOS expression levels across all subjects [17, 18]. We then computed an inter-regional
267 correlation matrix of C-FOS levels across all subjects for each experimental group. The inter-
268 regional correlation coefficient of C-FOS levels, r, was considered meaningful if its significant
269 correlation level P was <0.05, otherwise r was set to zero to reflect no correlation. For all inter-
270 regional pairs displaying a significant correlation, we identified large proportions of inter-
271 regional pairs with positive correlations and comparable positive r values among the four
272 experimental groups of WT ctrl, *Tbr1*$^{+/-}$ ctrl, WT TBS and *Tbr1*$^{+/-}$ TBS, yet very few but
273 variable inter-regional pairs exhibiting negative correlations in the WT ctrl (1.52%), *Tbr1*$^{+/-}$ ctrl
274 (2%), WT TBS (2.36%) and *Tbr1*$^{+/-}$ TBS (0.03%) groups (**Figure 5A**). Upon examining the
275 entire inter-regional correlation matrix, we observed that meaningful functional connections
276 between brain regions in *Tbr1*$^{+/-}$ mice in the awake state were noticeably reduced compared to
277 their WT littermates (**Figure 5B**, WT ctrl vs. *Tbr1*$^{+/-}$ ctrl). After TBS, inter-regional functional
278 connections were noticeably reduced in the wild-type group (**Figure 5B**, WT ctrl vs. WT TBS),
279 whereas they were dramatically increased in *Tbr1*$^{+/-}$ mice (**Figure 5B,** *Tbr1*$^{+/-}$ ctrl vs. *Tbr1*$^{+/-}$
280 TBS). Therefore, the opposing consequences caused by BLA activation in WT and *Tbr1*$^{+/-}$ mice

281 are not only reflected in neuronal recruitment of individual structures, but they are also
282 manifested by inter-regional functional connectivity.

283 Next, we quantified the degree centrality (DC) of each brain region based on our inter-
284 regional C-FOS correlation data (**Figure 5C**). A higher DC for a specific region indicates that
285 the activity of that region is synchronous with more brain regions. Our results show that the
286 WT ctrl group had a higher DC degree than the *Tbr1*$^{+/-}$ ctrl group. However, BLA activation
287 generally reduced DC degree in WT mice, but increased it in *Tbr1*$^{+/-}$ mice (**Figure 5C**). Thus,
288 the WT ctrl group was more synchronous than the *Tbr1*$^{+/-}$ ctrl group, and TBS at the BLA has
289 opposing effects in this respect on WT and *Tbr1*$^{+/-}$ mice.

290 In order to confirm that the differences in DC were not caused by the particular
291 correlation criteria we used, we evaluated the network stability of the four experimental groups
292 by increasing the r (correlation coefficient) or *P* (correlation significance) threshold used for
293 constructing the inter-regional correlation network (**Figure 5D**). Compared to the WT ctrl
294 network, the reduced mean DC of the *Tbr1*$^{+/-}$ ctrl network still existed across all the absolute r
295 and large range of *P* threshold conditions. Moreover, the contrasting modulatory effects of
296 BLA-derived circuit activation on DC between the wild-type and *Tbr1*$^{+/-}$ networks also existed
297 when all the absolute r and large range of *P* value thresholds were used for network construction
298 (**Figure 5D**). These results support that the differences in DC among the four experimental
299 groups are unbiased.

300

301 **Differential modular organization and reorganization upon BLA activation**

302 To understand which brain regions are more densely interconnected than others and to achieve
303 better modular integration, we used a Louvain community detection algorithm [19] to analyze
304 modular organization. Optimal communities were defined by C-FOS levels of the brain regions
305 being more correlated to each other within a community than between communities. We used
306 a spatial resolution parameter series, R, ranging from 0.4 to 0.9, in Louvain community
307 detection and calculated the difference in the modularity metric (Q) for communities
308 representing real networks or shuffled networks. The appropriate R-value for each network was
309 determined according to the maximal difference between Q and $Q_{shuffled}$ (**Figure 6A**).

310 Louvain community detection revealed distinct modular organizations for the four
311 experimental groups. The WT ctrl network contained 14 communities, with the majority of
312 brain regions occupying the first 3 communities (598/618 brain regions). The remaining
313 communities of the WT ctrl network comprised a few inter-correlated regions (communities 4,
314 6, 8, 9) or single brain regions (communities 5, 7, 10, 11, 12, 13, 14) (**Figures 6B, 6C**). In

315 contrast, the *Tbr1*$^{+/-}$ ctrl network only comprised four communities (**Figures 6B, 6C**). Indeed,
316 it was clear that none of the communities identified in the WT ctrl group were identical to those
317 of the *Tbr1*$^{+/-}$ ctrl group, no matter whether brain regions or mean correlation within or between
318 communities was being considered (**Figures 6B, 6C, Figure S7D, Table S3**).
319 Under BLA activation, the communities in the WT and *Tbr1*$^{+/-}$ mice were substantially
320 reorganized. All major communities of the WT TBS network (communities 1–3, total 613/618
321 regions) displayed weaker mean correlations within and between communities relative to the
322 first three communities of the WT ctrl network (**Figures 6B, 6C**, WT TBS communities 1-3 vs.
323 WT ctrl communities 1-3). For the *Tbr1*$^{+/-}$ TBS network, the brain regions were highly
324 concentrated in two communities, i.e., communities 1 and 3 (**Figures 6B, 6C**), with strong mean
325 within and between community correlations. Note that community 1 of *Tbr1*$^{+/-}$ TBS network is
326 similar to community 2 of WT ctrl network (**Figure 6C**), suggesting that amygdala activation
327 may reorganize neural network of *Tbr1*$^{+/-}$ mice to be more comparable to that in WT mice.
328 Overall, this community analysis suggests that Tbr1 haploinsufficiency reorganizes how
329 the mouse brain is networked and also leads to differential connectivity upon BLA activation.
330

331 ***Tbr1* deficiency and BLA activation influence the default mode network**

332 Finally, we applied our dataset to a physiologically relevant subnetwork analysis to explore any
333 differences among experimental groups. Our control groups reflect a cognitive state where the
334 mice were in their home cages during wakefulness and in the absence of any salient stimuli.
335 Therefore, we adopted the default mode network (DMN) as the most appropriate for our
336 analysis since it was initially identified by resting-state fMRI (functional magnetic resonance
337 imaging) as a set of brain regions with correlated activities in the absence of goal-directed tasks
338 and inactivation during task execution [20]. Since the DMN has been implied in social
339 behaviors and ASD [21, 22], DMN analysis likely provide more understanding about the
340 deficits in *Tbr1*$^{+/-}$ mice.
341 The core DMN regions in the mouse brain are located in the isocortical prefrontal
342 (ACAd, ACAv, PL, ILA, ORBl, ORBm, ORBvl), somatomotor (SSp-tr, SSp-ll, MOs) and
343 medial (VISa, VISam, RSPagl, RSPd, RSPv) areas of both brain hemispheres [23]. We
344 extracted our data on oChIEF patterns, C-FOS expression and functional connectivity for these
345 core DMN regions and compared them among our experimental groups. To aid visualization,
346 the summarized signals in 10 and 100 mm^3 cubes were used to highlight differences in oChIEF-
347 Citrine and C-FOS expression, respectively.

348 Among the DMN regions, *Tbr1*$^{+/-}$ mice exhibited more ipsilateral BLA projections,
349 especially in the ventral part of the ipsilateral ACA (i_ACAv), compared to wild-type mice
350 (**Figure 7A**, DMN ΔoChIEF), implying a role for TBR1 in controlling BLA axonal projections
351 into the DMN. For C-FOS expression, we observed more cubes with higher C-FOS^{+} cell
352 numbers in bilateral DMN regions for the *Tbr1*$^{+/-}$ ctrl vs. WT ctrl and WT TBS vs. WT ctrl
353 comparisons (**Figure 7B**). In contrast, there were more cubes with reduced numbers of C-FOS^{+}
354 cells for the *Tbr1*$^{+/-}$ TBS vs. *Tbr1*$^{+/-}$ Ctrl and *Tbr1*$^{+/-}$ TBS vs. WT TBS comparisons (**Figure**
355 **7B**). Thus, DMN activity is indeed sensitive to *Tbr1* deficiency and BLA activation.
356 We also determined the DC and participation coefficient (PC) of all DMN regions. PC
357 measures the relative distribution of a given brain region's (node) correlations (edges) with
358 other communities versus the correlations within its own community. Many regions of the
359 *Tbr1*$^{+/-}$ ctrl DMN exhibited reduced DC, and only the ipsilateral ACAv (i_ACAv) presented a
360 slightly elevated DC (**Figure 7C**). This outcome is likely relevant to the greater BLA axonal
361 innervation of the i_ACAv in the *Tbr1*$^{+/-}$ ctrl group (**Figure 7A**). In contrast to our findings for
362 DC, *Tbr1*$^{+/-}$ ctrl DMN regions showed elevated PC values for many regions relative to the WT
363 ctrl DMN (**Figure 7C**). These analyses again evidence that the connectivity of DMN in *Tbr1*$^{+/-}$
364 ctrl mice is abnormal, thus resembling the aberrant DMN displayed by ASD patients [24, 25].
365 We also observed that BLA activation elicited alterations to the DMN in both wild-type
366 and *Tbr1*$^{+/-}$ mice, albeit with different consequences (**Figure 7C**). In wild-type mice, BLA
367 activation induced the same decreasing tendency for DC in many of the DMN regions, but
368 various changes in PC (**Figure 7C**, WT TBS vs. WT ctrl). In *Tbr1*$^{+/-}$ mice, the same stimulation
369 treatment elevated DC but reduced PC in many of the DMN regions (**Figure 7C**, *Tbr1*$^{+/-}$ TBS
370 vs. *Tbr1*$^{+/-}$ ctrl). These differences in the DMN between wild-type and *Tbr1*$^{+/-}$ mice upon BLA
371 activation clearly demonstrate the differential responses of DMN regions to BLA activation
372 (**Figure 7C,** *Tbr1*$^{+/-}$ TBS vs. WT TBS).
373 Finally, we examined the reciprocal C-FOS correlation within different DMN regions
374 to visualize the inter-connected networks of the specific DMN regions (**Figure 7D**). Consistent
375 with a previous study on the mesoscopic mouse DMN [23], our wild-type mice exhibited a
376 strong inter-connected network among DMN regions (**Figure 7D**). However, the DMN of
377 awake *Tbr1*$^{+/-}$ mice (*Tbr1*$^{+/-}$ ctrl) had a much more loosely connected network, showing overall
378 hypoconnectivity (**Figure 7D**). TBS of the BLA again exerted opposing effects on *Tbr1*$^{+/-}$ mice
379 and their wild-type littermates, with the WT TBS group having a loosely connected network,
380 whereas the inter-connected network of the *Tbr1*$^{+/-}$ TBS group became stronger than that of
381 *Tbr1*$^{+/-}$ ctrl mice (**Figure 7D**).

382 Thus, using DMN as an example, our analyses support that Tbr1 deficiency and BLA
383 activation regulate the connectivity of physiologically relevant circuits.
384
385 **Discussion**
386 Using a whole-brain mapping and quantification system, we investigated the structure and
387 functional rewiring of BLA-derived circuits in a *Tbr1* ASD mouse model based on BLA axonal
388 projection patterns and C-FOS expression. We show impairment of contralateral projection and
389 ipsilateral mistargeting of BLA neurons in our *Tbr1*$^{+/-}$ mice, consequently altering global neural
390 activity under both control and TBS-mediated BLA activation conditions. We also observed
391 that whole-brain synchronization is altered by *Tbr1* deficiency, with or without BLA activation
392 (**Figure 8**). Our system provides a high-resolution method for analyzing functional connectivity
393 at the cellular level, which is a much more accurate approach compared to fMRI, even though
394 temporal resolution is not achievable in our system. To our knowledge, ours is the first study
395 to provide evidence in an ASD mouse model that particular circuit activation elicits differential
396 functional consequences in the mutant mice compared to wild-type mice subjected to the same
397 manipulation.
398 Altered local and long-range functional connectivity is one of the primary features of
399 ASD [26-29]. Mouse models have also been shown to recapitulate the connectivity deficits
400 displayed by human patients [27, 30-35]. *TBR1* deficiency is a particularly interesting case
401 because one of the outcomes, i.e., impairment of the anterior commissure, is shared by both
402 mouse and human [9-13]. Interamygdalar projections of BLA neurons into the two brain
403 hemispheres are defective in cases of *Tbr1* deficiency [7, 13]. In the current report, we have
404 further demonstrated that BLA axons in *Tbr1*$^{+/-}$ mice barely cross the midline between brain
405 hemispheres and mainly mistarget to ipsilateral brain regions. Although we have identified
406 several ipsilateral brain regions with more axonal projections from the ipsilateral BLA, our
407 PCA analysis indicates that many ipsilateral target regions exhibit considerable inter-sample
408 variability, indicating that some ipsilateral projections tend to be random and less specific. Our
409 work further highlights abnormal network synchronization, both at the whole-brain scale and
410 within a specific subnetwork (i.e., the DMN), in *Tbr1* mutant mice, providing the role of DMN
411 in an ASD mouse model.
412 The default mode network (DMN), originally defined by resting-state fMRI in human,
413 is highly relevant to ASD [22, 24, 25, 36, 37]. DMN abnormality results in atypical information
414 integration, prompting social-cognitive deficits [22, 37]. Unlike in humans, there are much
415 fewer studies on DMN in ASD mouse models [38, 39]. Here, we show that *Tbr1* deficiency

416 alters the structural and functional connectivity between the BLA and DMN. Moreover, BLA
417 activation results in opposing consequences for *Tbr1*$^{+/-}$ mice and wild-type littermates in terms
418 of neuronal activity and inter-network connectivity of the DMN. Similar to global brain
419 synchronization, TBS-induced BLA activation elicits stronger connectivity among regions of
420 the DMN in *Tbr1*$^{+/-}$ mice, thereby likely improving DMN function.
421 Our previous study showed that bilateral infusion of D-cycloserine, a coagonist of
422 NMDA receptor, into the BLA improved the social behaviors and associated memory of *Tbr1*$^{+/-}$
423 mice [7, 12], revealing a beneficial effect of BLA activation on *Tbr1*$^{+/-}$ mice. Consistently, here,
424 we found that TBS-mediated BLA activation globally increased correlations of C-FOS
425 expression among different brain regions, thus contributing to whole-brain synchronization.
426 This outcome implies that deep brain stimulation at the BLA likely improves the deficits caused
427 by *Tbr1* deficiency, consistent with previous studies indicating that deep brain stimulation
428 ameliorates autism phenotypes [40-42].
429
430 **Methods**
431 **Ethics statement**
432 All animal experiments were performed with the approval of the Academia Sinica Institutional
433 Animal Care and Utilization Committee and in strict accordance with its guidelines (Protocol
434 No. 14-11-759 and 18-10-1234). Human subject study is not included in the current work.
435
436 **Mice**
437 The *Tbr1*$^{+/-}$ mice were originally provided by Drs. J. L. Rubenstein (Department of Psychiatry,
438 University of California, San Francisco) and R. F. Hevner (Department of Neurological Surgery,
439 University of Washington, Seattle). *Tbr1*$^{+/-}$ mice and wild-type littermates were housed in the
440 animal facility of the Institute of Molecular Biology, Academia Sinica, under controlled
441 temperature and humidity and a 12 h light/12 h dark cycle. All animal experiments were
442 performed at 3-5 months of age with the approval of the Academia Sinica Institutional Animal
443 Care and Utilization Committee and in strict accordance with its guidelines (Protocol No. 14-
444 11-759 and 18-10-1234).
445
446 **Virus production**
447 For axon tracing and *in vivo* stimulation of BLA-derived circuits, we packaged an adeno-
448 associated virus (AAV) that expresses the ultra-fast channelrhodopsin (ChR) variant oChIEF-
449 Citrine under the control of the human Synapsin promoter (AAV-Syn-oChIEF-Citrine) as

450 described in our previous study [13]. Briefly, a transgenic plasmid encoding oChIEF-Citrine,
451 AAV helper plasmid serotype AAV8 capsid and AAV2 replication proteins, together with an
452 adenovirus helper plasmid encoding essential proteins for AAV packaging were transfected
453 into adenovirus E1-expressing cells. Crude virus soup was obtained from transfected E1-
454 expressing cells and purified by iodixanol gradient centrifugation. The physical vector titers
455 were quantified by measuring the number of packaged vector genomes by real-time PCR using
456 SYBR Green reaction mix (Roche Diagnostics, Mannheim, Germany).
457
458 **Experimental procedure of the mesoscopic whole-brain scale circuit analysis pipeline**
459 In order to analyze the structural and functional connectivity of BLA-derived circuits, we
460 developed a mesoscopic whole-brain scale circuit analysis pipeline (**Figure 1 and Figure S1**).
461 Detailed methods are described in the following sections.
462
463 *Step1: Brain sample preparation*
464 To label the BLA-derived circuits and manipulate their activity for examining functional
465 consequences, we performed stereotaxic surgeries for virus infection and optic fiber
466 implantation. Mice were deeply anesthetized and their heads were secured on a Lab Standard™
467 Stereotaxic Instrument (Stoelting, Wood Dale, IL USA). AAV-Syn-oChIEF-Citrine (0.1 μl,
468 10^{10} genomes/μl) was slowly infused over 10 min unilaterally into the BLA (virus injection
469 coordinates: 1.3 mm posterior, 3.3 mm lateral and 4.95 mm ventral to the bregma). Upon
470 completing virus injection, an optic fiber was slowly inserted into the site to 0.05 mm above
471 the virus injection site (optic fiber implantation coordinates: 1.3 mm posterior, 3.3 mm lateral
472 and 4.9 mm ventral to the bregma).
473 After recovering for at least 3 weeks, the mice were habituated to being hand-held, to
474 having a patch cable connected to the optic fiber, and to the lid of their home cage being opened
475 for 10 minutes when the patch cable was being connected. Habituation sessions were conducted
476 once per day for 3 days. *In vivo* optogenetic simulation and brain sample fixation were carried
477 out on the day following the last habituation session. We used a 473 nm laser with 10 mW light
478 intensity (emitted from the tip of the optic fiber) for optogenetic stimulation. After 10 min of
479 freely exploring their home cage, mice received five repetitive theta burst frequency
480 stimulations (TBS: 10 trains/TBS, inter-train interval, 200 ms; 5 pulses/train, inter-pulse
481 interval, 10 ms) with a 30 s inter-TBS interval to a unilateral BLA. This experimental
482 stimulation paradigm mimics physiological theta oscillations and has been demonstrated to
483 intensify responses to cortical and thalamic inputs through commissural BLA projections [13].

484 TBS was also used to induce changes in neuronal plasticity of the BLA [43]. Therefore, the
485 functional consequences of TBS on BLA-derived circuits can persist and prevail over the
486 random activation of BLA neurons during wakefulness. After photostimulation or sham
487 manipulation (without light emission), mice were kept in their home cage for 2 hr until sacrifice
488 by perfusing them with 4% paraformaldehyde in PBS. The brains were then dissected out and
489 post-fixed overnight at 4 °C.
490
491 *Step2: High-content immunofluorescence imaging*
492 Brains were cryopreserved in 30% sucrose at 4 °C for 2 days and then embedded in OCT (4583,
493 Tissue-TeK). For whole-brain analysis, we used a cryostat microtome (CM1900, Leica) to
494 cryosection each brain from the posterior to anterior cerebrum into at least 120 consecutive
495 coronal brain slices (60 μm/slice), with the cerebellum and olfactory bulb being excluded from
496 our analysis. Traditional immunohistochemical methods were deployed, as described
497 previously [13]. Primary anti-GFP (1:5000, Abcam) and anti-C-FOS (1:200, Cell Signaling)
498 antibodies were used to reveal Citrine-containing BLA axonal projections and C-FOS
499 immunoreactivities, respectively. The stained coronal brain sections (at least 120 sections) with
500 intensified oChIEF-Citrine (stained with GFP antibody) and C-FOS (stained with C-FOS
501 antibody) signals were imaged with a high-content imaging system (Molecular Devices)
502 hosting a 4x objective. Images from one brain were stitched together using MetaXpress
503 6.2.3.733 (Molecular Devices) and manually aligned in Amira 6.4 (ThermoFisher Scientific)
504 or Etomo [44].
505
506 *Step3: Registration and transformation to Allen Mouse Common Coordinate Framework*
507 *version 3 (CCFv3)*
508 After acquiring the aligned consecutive slice raw images, we registered image series to CCFv3
509 [15]. We downloaded high-resolution coronal templates with a 10 μm resolution along the
510 anterior-posterior (AP) axis using Allen Software Development Kit Python code, and then
511 manually matched the corresponding template to each raw image according to certain landmark
512 brain structures, such as the beginning and end of the hippocampus (HIP), the location of the
513 anterior commissure (act and aco), and the disconnections of the corpus callosum (cc). After
514 determining the matched template for each raw image, binary experimental images were
515 registered to the matched binary templates by means of the medical image registration library
516 SimpleElastix [45], first with 12 global (translation and affine) and then one local (B-spline)

517 transforming parameters. Finally, the stored multiple transforming parameters were applied to
518 merge the experimental images of oChIEF-Citrine and C-FOS signals into registered images.
519
520 *Step4: Image segmentation for oChIEF and C-FOS signals (also see **Figure S1**)*
521 Before quantification of oChIEF and C-FOS signals and comparing the differences between
522 wild-type and *Tbr1*$^{+/-}$ mice, we needed to eliminate fluorescence signals due to experimental
523 variation and background interference. The purpose of image segmentation for oChIEF signals
524 was to determine which pixels are oChIEF-positive (**Figure S1A**). Therefore, first we deployed
525 the pixel classification algorithm ilastik1.3.3 [46] to predict the probability that every pixel in
526 a registered image displayed oChIEF signals. The oChIEF probability maps of each image were
527 cross-referenced against the registered images pixel by pixel. The resulting filtered images (raw
528 signal intensity x probability) were further processed to intensify edges by subtracting the
529 Gaussian blurred version of the filtered images. The edge-enhanced filtered images were then
530 subjected to thresholding/binarization (>6x S.D. of the Z-stacked image with filtering and edge
531 enhancement) to isolate oChIEF-positive pixels.
532 The aim of image segmentation for C-FOS signals was to determine the locations of
533 C-FOS^{+} cells within each image (**Figure S1B**). We preprocessed the raw C-FOS images by
534 applying rolling-ball background subtraction (ImageJ, radius 50 pixels). The spot detection
535 algorithm of Imaris 9.3 (Bitplane) was then applied to detect C-FOS^{+} cells from background-
536 subtracted images using consistent criteria (Detection spot diameter: 10 μm; Detection
537 threshold: 2 x S.D. of the Z-stacked image with background subtraction). The locations of C-
538 FOS^{+} cells in each image could then be exported. Finally, the binarized oChIEF signals and C-
539 FOS^{+} cell locations of each registered image were subjected to quantification.
540
541 *Step5: Application of brain structure masks and quantification of oChIEF and C-FOS signals*
542 We accessed the Reference Space of CCFv3 to obtain the coronal indicator masks of each brain
543 region by using Allen Software Development Kit Python code. The coronal indicator masks
544 could separately compartmentalize oChIEF-positive pixels and C-FOS^{+} cells into different
545 brain regions, which served as regions of interest (ROI) to quantify the binarized oChIEF
546 percentage or C-FOS^{+} cell number for each brain region along the AP axis. All computations
547 were carried out using the Numpy, Pandas, OpenCV, scikit-image and GeoPandas Python
548 packages. The data compartmentalizing oChIEF-positive pixels and C-FOS^{+} cells into different
549 brain regions were subsequently used for 3D visualization. Data on quantified oChIEF
550 percentage, C-FOS^{+} cell numbers, and brain region area were used for the analysis. Some brain

551 regions were excluded from the analysis of oChIEF signals, such as ipsilateral BLA-related
552 regions (LA, BLA, BLAa, BLAp) and bilateral VISam, which contained artificial signals
553 caused by experimental surgery for virus injections. Moreover, the bilateral somatosensory
554 cortex (SSp, SSp-n, SSp-bfd, SSp-ll, SSp-tr, SSp-un, SSs) and corpus callosum-related fiber
555 tracts (cc, fa, ec, ee, ccb, ccs) were also excluded from the analysis due to exiguous oChIEF-
556 Citrine-expressing AAV infections during surgery.
557
558 **k-nearest neighbors (KNN) algorithm-based classification**
559 To examine the spatial separability of virus injection sites or PC locations in a PCA analysis,
560 we conducted a KNN-based classification with five-fold cross-validation using scikit-learn
561 Python package. A series of numbers of nearest neighbors was used to identify the one
562 achieving the best KNN classification accuracy. Furthermore, a randomized dataset of virus-
563 injecting locations or PC locations, shuffled 1000 times, between experimental groups was used
564 to validate the significance of spatial separability. The spatial separability was considered
565 significant when the KNN classification accuracy of the real dataset deviated from the same
566 metric distribution calculated for the randomized dataset ($P < 0.05$).
567
568 **Volume-based quantification and related analysis**
569 Volume-based quantification of oChIEF signals allowed us to calculate the percentage of
570 oChIEF signals (%) in a given brain region volume. To do this, total numbers of oChIEF pixels
571 within a brain region were calculated first by summing over all oChIEF pixels in single slices
572 (products of quantified oChIEF percentage and region area) belonging to the same region along
573 the AP axis and then dividing by the sum of the region area along the AP axis. Volume-based
574 quantification of C-FOS signals revealed the density of C-FOS$^+$ cells in a given brain region
575 volume (cells/mm^3). To calculate these values, total C-FOS$^+$ cells within a brain region were
576 calculated first by summing over all C-FOS$^+$ cells in single slices and then dividing by the
577 volume of the brain region (converted to mm^3). Volume-based quantification data for oChIEF
578 and C-FOS signals were used in structure-wise comparisons (both oChIEF and C-FOS data),
579 principal component analysis (PCA; oChIEF data), and network analysis of inter-regional C-
580 FOS correlations (C-FOS data), all described further below.
581
582 *Structure-wise comparison of volume-based quantification data (also see **Figure S3A**)*
583 Before undertaking structure-wise comparisons of oChIEF percentages or C-FOS cell densities
584 between different experimental groups (oChIEF data: WT and *Tbr1*$^{+/-}$; C-FOS data: WT ctrl,

585 *Tbr1*$^{+/-}$ ctrl, WT TBS and *Tbr1*$^{+/-}$ TBS), we set a threshold for selecting brain regions for the
586 comparisons. To compare oChIEF percentages, brain regions with a oChIEF percentage greater
587 than the 20th percentile in all *Tbr1*$^{+/-}$ regional quantifications were selected (257 contralateral
588 and 357 ipsilateral brain regions). For C-FOS^{+} cell density comparison, brain regions with a
589 summed C-FOS cell density for all experimental groups (WT ctrl, *Tbr1*$^{+/-}$ ctrl, WT TBS and
590 *Tbr1*$^{+/-}$ TBS) greater than 800 cells/mm^3 were selected (311 contralateral and 307 ipsilateral
591 brain regions). All the data on each brain region were normalized to the respective averaged
592 WT (oChIEF data) or WT ctrl (C-FOS data) values before being subjected to statistical analysis.
593 For the structure-wise oChIEF comparison, a two-sided Mann-Whitney U test was conducted
594 in the SciPy sub-package scipy.stats. For the structure-wise C-FOS comparison, a Kruskal-
595 Wallis test was conducted (using scipy.stats), followed by a post-hoc Dunn test with Bonferroni
596 adjustment of *P* value (using the scikit-posthocs Python package) if the Kruskal-Wallis test was
597 significant ($P < 0.05$).
598
599 *Structure-wise comparison of the ratio of contralateral Citrine signal to ipsilateral Citrine*
600 *signal (the C/I ratio) from volume-based quantification data*
601 The brain regions selected for C/I ratio comparison were those displaying a significant oChIEF
602 percentage (above the defined threshold) in both brain hemispheres in wild-type samples. The
603 C/I ratio data were normalized to the averaged C/I ratio of wild-type samples. The structure-
604 wise C/I ratio comparison was also conducted by two-sided Mann-Whitney U test using
605 scipy.stats.
606
607 *PCA analysis of oChIEF signals*
608 To visualize differences in oChIEF percentages across all brain regions and between wild-type
609 and *Tbr1*$^{+/-}$ mouse brains, we conducted a PCA analysis on the oChIEF percentage data using
610 the scikit-learn. Per-sample data across all brain regions were projected onto the first two
611 principal components.
612
613 *Network analysis of inter-regional C-FOS correlations*
614 Functional connectivity, as measured in our study, was based on synchronization of C-FOS
615 expression levels between two brain regions in individual subjects. Therefore, we used relative
616 C-FOS density (normalized to the averaged value for WT ctrl) obtained from our volume-based
617 quantification data as a single metric to represent the C-FOS level of a given brain region of
618 one sample. To measure all possible synchronizations, we evaluated inter-regional C-FOS

619 correlations between all possible brain region pairs by means of two-sided Kendall's rank
620 correlation (using scipy.stats) across all the samples in the same experimental group. A network
621 of inter-regional C-FOS correlations was constructed using the significant C-FOS correlations
622 (edges, significance level $P < 0.05$) between brain region pairs (nodes) by using the NetworkX
623 Python package. Self-to-self correlations were removed. The degree centrality (DC) and
624 participation coefficient (PC) of individual nodes (brain regions) were calculated using
625 NetworkX.
626 To dissect the modular organization of networks, we adopted a Louvain community detection
627 algorithm and the modularity metric (Q) calculation provided by NetworkX. To identify the
628 optimal resolution parameter R value used for Louvain community detection, we generated a
629 shuffled network by maintaining the same correlation weights (edges) while randomizing the
630 source and target regions (nodes). An R value series (0.4 to 0.9 in steps of 0.1) was used for
631 Louvain community detection of real and shuffled networks. For each R value, the difference
632 in Q between the modularity of the real network and the shuffled network was calculated 1000
633 times. The most appropriate R value that generated the maximal mean difference of Q ($Q-$
634 $Q_{shuffled}$) was selected for Louvain community detection. These computations were achieved
635 using Numpy, Pandas and NetworkX.
636
637 **Slice-based quantification and related analysis**
638 Slice-based quantifications of oChIEF and C-FOS signals involved calculating the oChIEF
639 pixel (products of quantified oChIEF percentage and region area) and C-FOS$^+$ cell distributions
640 along the AP axis, respectively. To achieve fair comparisons, we carried out 100 μm binning
641 of oChIEF pixel and C-FOS$^+$ cell distributions along the AP axis. The binned oChIEF pixel and
642 C-FOS$^+$ cell distributions were then used for structure-wise comparisons and correlation
643 analysis between rewired BLA-derived circuits and their C-FOS modulatory ability.
644
645 *Structure-wise comparison of the data from slice-based quantification (also see **Figure S6A**)*
646 Before structure-wise comparison of oChIEF pixel or C-FOS$^+$ cell distributions between
647 different groups (oChIEF data, WT and *Tbr1*$^{+/-}$; C-FOS data, WT ctrl, *Tbr1*$^{+/-}$ ctrl, WT TBS
648 and *Tbr1*$^{+/-}$ TBS), we set a threshold to select brain regions for comparison. To compare
649 oChIEF pixel distributions, brain regions were selected with a summed total oChIEF pixels for
650 both groups (WT + *Tbr1*$^{+/-}$) greater than 13-fold the standard deviation of all oChIEF pixels in
651 all contralateral brain regions (207 contralateral and 344 ipsilateral brain regions). To compare
652 C-FOS$^+$ cell distributions, brain regions with a summed total C-FOS$^+$ cells for all compared

653 groups (WT ctrl, *Tbr1*$^{+/-}$ ctrl, WT TBS and *Tbr1*$^{+/-}$ TBS) greater than 100 cells were selected
654 (313 contralateral and 311 ipsilateral brain regions). For our structure-wise comparisons of
655 oChIEF pixel and C-FOS^{+} cell distributions along the AP axis, Friedman's one-way repeated
656 measure analyses were conducted using the Pingouin Python package. A post-hoc
657 nonparametric pairwise test with one-step Bonferroni correction of *P* value (using Pingouin)
658 was conducted for the C-FOS^{+} cell distributions if the outcome of the Friedman one-way
659 repeated measure analysis was significant ($P < 0.05$). To express the extent of distributional
660 differences between compared groups, we conducted pair-wise subtractions of the oChIEF
661 pixels or C-FOS^{+} cell numbers for the same AP coordinates between all possible pairs. The
662 differences along the AP axis of all sample pairs were then averaged and summed into single
663 metrics (sum of ΔoChIEF or sum of ΔC-FOS) to represent the extent of any differences.
664
665 *Correlation analysis of rewired BLA-derived circuits and their C-FOS modulatory ability*
666 Brain regions selected for correlation analysis were those receiving differential BLA axonal
667 innervations between wild-type and *Tbr1*$^{+/-}$ mouse brains (Friedman test P value < 0.05) and
668 altered C-FOS^{+} cell distributions upon TBS-mediated BLA activation in either wild-type or
669 *Tbr1*$^{+/-}$ mice (adjusted P value <0.05 in WT TBS vs. WT ctrl or *Tbr1*$^{+/-}$ TBS vs. *Tbr1*$^{+/-}$ ctrl).
670 First, we determined ΔoChIEF traces by pairwise subtraction of oChIEF-Citrine signals
671 between *Tbr1*$^{+/-}$ and wild-type samples. The neural activation induced by TBS in *Tbr1*$^{+/-}$ mice
672 and WT littermates, i.e., WT ΔC-FOS traces and *Tbr1*$^{+/-}$ ΔC-FOS traces, was also determined.
673 Pairwise subtraction between *Tbr1*$^{+/-}$ ΔC-FOS traces and WT ΔC-FOS traces was then executed
674 to obtain all possible differences, i.e., ΔΔC-FOS traces. A Pearson correlation coefficient (r)
675 was calculated between the averaged ΔoChIEF trace and the averaged ΔΔC-FOS trace for each
676 brain region. To determine if any correlation was meaningful, i.e., distinct from non-correlated
677 pairs, the order of ΔoChIEF traces, WT ΔC-FOS traces and *Tbr1*$^{+/-}$ ΔC-FOS traces along the
678 AP axis was independently reshuffled 1000 times to create 1000 putatively non-correlated mean
679 ΔoChIEF and mean ΔΔC-FOS shuffled pairs. We defined that a meaningful positive or negative
680 correlation between mean ΔΔoChIEF and ΔΔC-FOS values should fit three criteria. First, the r
681 value should deviate from the same metric obtained from the shuffled dataset ($r_{shuffled}$) (positive
682 correlation, above 95% $r_{shuffled}$ distribution; negative correlation, below 95% $r_{shuffled}$ distribution).
683 Second, the r value should be >0.1 (positive correlation) or <–0.1 (negative correlation). Third,
684 the tendency thresholds of ΔoChIEF and ΔΔC-FOS traces were determined according to the
685 mean 99th percentiles of scaled differences, which were calculated from the pair-subtraction

686 population dataset with 1000 times AP axis reshuffling (**Figures 4B, 4D**, dashed line in middle
687 panel). A positive or negative correlation between mean ΔoChIEF and ΔΔC-FOS depended on
688 the product of ΔoChIEF and ΔΔC-FOS tendency thresholds (positive correlation, > 0; negative
689 correlation, <0). The computations of all correlation analyses were carried out using Pandas
690 and Numpy.
691
692 **ROI corrections of brain region masks**
693 We selected 44 contralateral and 50 ipsilateral brain regions for manual correction of the
694 mismatched ROI in every single brain slice image of each brain sample. To do this, the original
695 coronal indicator masks of each brain region were separated into contralateral and ipsilateral
696 masks and converted to ImageJ ROIs by sequentially applying the ImageJ Create Selection
697 function and adding it to ImageJ ROI Manager. Using the C-FOS or oChIEF raw images
698 (registered to CCFv3) as references, ROIs were verified and corrected by manually adjusting
699 their shapes and locations. After ROI corrections, the ROIs of each brain region in both
700 hemispheres were converted back to image masks by applying the ImageJ Create Mask function.
701 The new coronal indicator masks were then used for re-quantifications.
702
703 **3D visualization**
704 *Summarized 3D stack of binarized oChIEF images*
705 To visualize differences in BLA-derived circuits between wild-type and *Tbr1*$^{+/-}$ mice, the
706 binarized oChIEF image series of individual brains was binned on the dorsal-ventral and
707 medial-lateral axis into 10 μm/pixel. Each binned pixel intensity represented the oChIEF
708 probability. The AP coordinates of the binned oChIEF image series were converted into the
709 respective CCFv3 coordinates (10 μm/pixel) and all binned oChIEF image series of individual
710 brains were then merged. If the same AP coordinate contained multiple binned oChIEF image
711 series from different brain samples, we conducted averaging on the intensity of those binned
712 oChIEF image series. If an AP coordinate contained only one binned oChIEF image, then that
713 binned image represented the oChIEF signals for that particular AP coordinate. The 3D stack
714 of binned and averaged oChIEF image series was adopted to illustrate BLA-derived circuits at
715 a whole-brain scale. Image processing was carried out using ImageJ, Numpy and scikit-image.
716
717 *3D mapping of binned BLA-derived circuits or C-FOS*$^{+}$ *cell distributions*

718 To visualize the innervations of BLA-derived circuits or the distributions of C-FOS$^+$ cells in
719 particular brain regions, we used the datasets on compartmentalized oChIEF-positive pixels and
720 C-FOS$^+$ cells for different brain regions. The CCFv3 whole brain shell was obtained from the
721 image stacks of CCFv3 "root" coronal indicator masks and converted to an isosurface mesh
722 with smoothing using the vedo Python package. For BLA-derived circuit visualization, binned
723 and averaged oChIEF image stacks within particular regions were employed and binned pixels
724 (10 μm^3 cubes) were converted into vectorized points using Numpy, Pandas and vedo. Each
725 vectorized point expressed different information, such as the brain region to which the point
726 belonged (discontinuous color map), scaled metrics expressing the difference between
727 compared groups (continuous color map), and oChIEF probability (alpha level). Vectorized
728 oChIEF points were mapped onto the 3D whole brain shell using vedo. To visualize C-FOS$^+$
729 cell distributions, the locations of C-FOS$^+$ cells were first binned by 100 μm^3 cubes in every
730 brain sample, and then the averaged C-FOS density of every 100 μm^3 cube was calculated
731 across brain samples of the same experimental group. Every binned and averaged C-FOS cube
732 (100 μm^3) within particular regions was converted into a vectorized sphere using Numpy,
733 Pandas and vedo. Each vectorized sphere expressed different information, such as the brain
734 region to which the sphere belonged (discontinuous color map), scaled metrics expressing the
735 difference between compared groups (continuous color map), and the normalized C-FOS
736 density within the cube (size of the sphere). Vectorized C-FOS spheres were mapped onto the
737 3D whole brain shell using vedo.
738
739 *3D mapping of C-FOS correlation networks among main brain areas*
740 To visualize the C-FOS correlation networks shown in **Figure 8**, the central locations of the
741 main cortical (prefrontal, somatomotor, medial, lateral, auditory and visual) and subcortical
742 areas (OLF, HPF, CTXsp, CNU, TH, HY, MB and HB) in both hemispheres were first
743 determined by averaging the locations of all the binned 100-μm^3 cubes belonging to particular
744 brain areas. Mean correlations within and between brain areas were then calculated. Centroids
745 representing particular brain areas in the ipsilateral or contralateral hemisphere were converted
746 to vectorized spheres using vedo. The color of each sphere represented brain area identity and
747 the size reflected mean correlation extent. To visualize inter-area mean correlations, correlation
748 edges were generated using vedo. For each edge, color represented correlational polarity and
749 thickness reflected mean correlation extent. Vectorized centroid spheres (brain areas) and inter-

750 area edges (inter-area mean correlations) were mapped onto a 3D whole brain shell again using
751 vedo.
752
753 **Quantification and statistical analysis**
754 Sample size n represents the number of brain samples from individual animals in each
755 experimental group. We did not use statistical methods to predetermine sample sizes, but our
756 sample size is similar to those brain connectome studies in previous publication [47]. Volume-
757 based quantification and its-associated analysis of oChIEF signals (KNN-based classification
758 of virus injection sites and PC locations, structure-wise comparisons, PCA analysis and C/I
759 ratio analysis) are based on n = 13 of wild-type (6 from WT ctrl and 7 from WT TBS groups)
760 and n = 15 of $Tbr1^{+/-}$ brain samples (7 from $Tbr1^{+/-}$ ctrl and 8 from $Tbr1^{+/-}$ TBS groups).
761 Volume-based quantification of relative C-FOS density and inter-regional C-FOS correlation
762 analysis was based on the brain samples largely overlapped with volume-based quantification
763 and analysis of oChIEF signals. We included one additional brain sample for both genotypes
764 which has mistargeted virus expression in the control condition and excluded one sample from
765 $Tbr1^{+/-}$ TBS due to inappropriate image acquisition of C-FOS signals. Brain samples used for
766 slice-based analysis (structure-wise comparisons and correlation analysis) are almost the same
767 as those used in the volume-based analysis of oChIEF signals, with the exclusion of one brain
768 sample from the $Tbr1^{+/-}$ TBS group which had inappropriate image acquisition of C-FOS
769 signals. The exact n numbers of experimental groups for every analysis can be found in figure
770 legends. For the data distribution, we did not use statistical methods to test data normality but
771 we assumed most of the quantified data is not normally distributed. Therefore, non-parametric
772 tests were used for statistical analysis. Statistical details can be found in the method sections
773 describing each analysis. Data representing statistical parameters such as mean ± SEM, median
774 and interquartile range are described in figure legends. All test statistics (e.g. exact *P* value,
775 Mann-Whitney U statistic, Friedman chi-square statistic, and degrees of freedom) of structure-
776 wise comparisons (volume-based or slice-based analysis) can be found in **Tables S1 and S2.**
777
778 **Declarations**
779 **Ethics approval and consent to participate**
780 Only mice were used in this study. All animal experiments were performed with the approval
781 of the Academia Sinica Institutional Animal Care and Utilization Committee (Protocol No. 14-

11-759 and 18-10-1234) and in strict accordance with its guidelines and those of the Council of Agriculture Guidebook for the Care and Use of Laboratory Animals.

Consent for publication

Not applicable.

Availability of data and materials

All sample data will be shared by the lead contact upon request. Custom code used for volume-based quantification, slice-based quantification, network analysis and 3D visualization has been uploaded to GitHub (https://github.com/HsuehYiPing/Tbr1Amyg).

Competing interests

The authors report no competing interests.

Funding

This work was supported by grants from Academia Sinica (AS-IA-106-L04 and AS-TP-110-L10 to Y.-P.H.), and the National Science and Technology Council (NSTC 112-2326-B-001-008 to Y.-P.H.). The funders had no role in study design, data collection and analysis, the decision to publish or the preparation of the manuscript.

Author contributions

Conceptualization, T.-T.H. and Y.-P.H.; Methodology and investigation, T.-T.H.; Coding, T.-T.H. and C.-Y.W.; Writing – original draft, T.-T.H. and Y.-P.H.; Writing – review and editing, T.-T.H., C.-Y.W. and Y.-P.H.; Funding acquisition, Y.-P.H.; Supervision and project administration, Y.-P.H. All authors contributed to the article and approved the submitted version.

Acknowledgments

We thank the Imaging Core and Animal Facility of the Institute of Molecular Biology, Academia Sinica, for technical assistance, Dr. John O'Brien for English editing and members of Y.-P.H.'s laboratory for technical assistance and discussion. This work was supported by grants from Academia Sinica (AS-TP-110-L10 and AS-IA-111-L01 to Y.-P.H.).

References

1. Geschwind DH, Levitt P. Autism spectrum disorders: developmental disconnection syndromes. Curr Opin Neurobiol. 2007;17(1):103-11. Epub 2007/02/06. doi: 10.1016/j.conb.2007.01.009.
2. Uddin L, Supekar K, Menon V. Reconceptualizing functional brain connectivity in autism from a developmental perspective. Frontiers in Human Neuroscience. 2013;7:458. doi: 10.3389/fnhum.2013.00458.
3. Di Martino A, Yan CG, Li Q, Denio E, Castellanos FX, Alaerts K, et al. The autism brain imaging data exchange: towards a large-scale evaluation of the intrinsic brain architecture in autism. Molecular Psychiatry. 2014;19(6):659-67. doi: 10.1038/mp.2013.78.
4. Ameis SH, Catani M. Altered white matter connectivity as a neural substrate for social impairment in Autism Spectrum Disorder. Cortex. 2015;62:158-81. doi: https://doi.org/10.1016/j.cortex.2014.10.014.
5. Bulfone A, Smiga SM, Shimamura K, Peterson A, Puelles L, Rubenstein JL. T-brain-1: a homolog of Brachyury whose expression defines molecularly distinct domains within the cerebral cortex. Neuron. 1995;15(1):63-78. PubMed PMID: 7619531.
6. De Rubeis S, He X, Goldberg AP, Poultney CS, Samocha K, Cicek AE, et al. Synaptic, transcriptional and chromatin genes disrupted in autism. Nature. 2014;515(7526):209-15. Epub 2014/11/05. doi: 10.1038/nature13772.
7. Huang TN, Chuang HC, Chou WH, Chen CY, Wang HF, Chou SJ, et al. Tbr1 haploinsufficiency impairs amygdalar axonal projections and results in cognitive abnormality. Nat Neurosci. 2014;17(2):240-7. Epub 2014/01/21. doi: 10.1038/nn.3626.
8. Chuang HC, Huang TN, Hsueh YP. T-Brain-1--A Potential Master Regulator in Autism Spectrum Disorders. Autism Res. 2015;8(4):412-26. Epub 2015/01/21. doi: 10.1002/aur.1456. PubMed PMID: 25600067.
9. Nambot S, Faivre L, Mirzaa G, Thevenon J, Bruel AL, Mosca-Boidron AL, et al. De novo TBR1 variants cause a neurocognitive phenotype with ID and autistic traits: report of 25 new individuals and review of the literature. Eur J Hum Genet. 2020. Epub 2020/02/02. doi: 10.1038/s41431-020-0571-6. PubMed PMID: 32005960.
10. Hsueh YP, Hsu TT, Huang TN. The evolutionarily conserved function of TBR1 in controlling the size of anterior commissure in human and mouse brains. Eur J Hum Genet. 2020;28(8):997-8. Epub 2020/04/11. doi: 10.1038/s41431-020-0621-0. PubMed PMID: 32273580.
11. Co M, Barnard RA, Jahncke JN, Grindstaff S, Fedorov LM, Adey AC, et al. Shared and Distinct Functional Effects of Patient-Specific Tbr1 Mutations on Cortical Development. J Neurosci. 2022;42(37):7166-81. Epub 2022/08/10. doi: 10.1523/jneurosci.0409-22.2022. PubMed PMID: 35944998; PubMed Central PMCID: PMCPMC9480892.
12. Huang TN, Yen TL, Qiu LR, Chuang HC, Lerch JP, Hsueh YP. Haploinsufficiency of autism causative gene Tbr1 impairs olfactory discrimination and neuronal activation of the olfactory system in mice. Mol Autism. 2019;10:5. Epub 2019/02/23. doi: 10.1186/s13229-019-0257-5. PubMed Central PMCID: PMCPMC6371489.
13. Huang TN, Hsu TT, Lin MH, Chuang HC, Hu HT, Sun CP, et al. Interhemispheric Connectivity Potentiates the Basolateral Amygdalae and Regulates Social Interaction and Memory. Cell Rep. 2019;29(1):34-48.e4. Epub 2019/10/03. doi: 10.1016/j.celrep.2019.08.082. PubMed PMID: 31577954.
14. Hsu T-T, Huang T-N, Hsueh Y-P. Anterior Commissure Regulates Neuronal Activity of Amygdalae and Influences Locomotor Activity, Social Interaction and Fear Memory in Mice. Frontiers in Molecular Neuroscience. 2020;13:47. doi: 10.3389/fnmol.2020.00047.

15. Wang Q, Ding S-L, Li Y, Royall J, Feng D, Lesnar P, et al. The Allen Mouse Brain Common Coordinate Framework: A 3D Reference Atlas. Cell. 2020;181(4):936-53.e20. doi: https://doi.org/10.1016/j.cell.2020.04.007.
16. Hintiryan H, Bowman I, Johnson DL, Korobkova L, Zhu M, Khanjani N, et al. Connectivity characterization of the mouse basolateral amygdalar complex. Nature Communications. 2021;12(1):2859. doi: 10.1038/s41467-021-22915-5.
17. Wheeler AL, Teixeira CM, Wang AH, Xiong X, Kovacevic N, Lerch JP, et al. Identification of a Functional Connectome for Long-Term Fear Memory in Mice. PLOS Computational Biology. 2013;9(1):e1002853. doi: 10.1371/journal.pcbi.1002853.
18. Rogers-Carter MM, Varela JA, Gribbons KB, Pierce AF, McGoey MT, Ritchey M, et al. Insular cortex mediates approach and avoidance responses to social affective stimuli. Nature Neuroscience. 2018;21(3):404-14. doi: 10.1038/s41593-018-0071-y.
19. Rubinov M, Sporns O. Complex network measures of brain connectivity: Uses and interpretations. NeuroImage. 2010;52(3):1059-69. doi: https://doi.org/10.1016/j.neuroimage.2009.10.003.
20. Raichle ME. The Brain's Default Mode Network. Annual Review of Neuroscience. 2015;38(1):433-47. doi: 10.1146/annurev-neuro-071013-014030. PubMed PMID: 25938726.
21. Nair A, Jolliffe M, Lograsso YSS, Bearden CE. A Review of Default Mode Network Connectivity and Its Association With Social Cognition in Adolescents With Autism Spectrum Disorder and Early-Onset Psychosis. Front Psychiatry. 2020;11:614. Epub 2020/07/17. doi: 10.3389/fpsyt.2020.00614. PubMed PMID: 32670121; PubMed Central PMCID: PMCPMC7330632.
22. Harikumar A, Evans DW, Dougherty CC, Carpenter KLH, Michael AM. A Review of the Default Mode Network in Autism Spectrum Disorders and Attention Deficit Hyperactivity Disorder. Brain Connect. 2021;11(4):253-63. Epub 2021/01/07. doi: 10.1089/brain.2020.0865. PubMed PMID: 33403915; PubMed Central PMCID: PMCPMC8112713.
23. Whitesell JD, Liska A, Coletta L, Hirokawa KE, Bohn P, Williford A, et al. Regional, Layer, and Cell-Type-Specific Connectivity of the Mouse Default Mode Network. Neuron. 2021;109(3):545-59. doi: https://doi.org/10.1016/j.neuron.2020.11.011.
24. Starck T, Nikkinen J, Rahko J, Remes J, Hurtig T, Haapsamo H, et al. Resting state fMRI reveals a default mode dissociation between retrosplenial and medial prefrontal subnetworks in ASD despite motion scrubbing. Frontiers in Human Neuroscience. 2013;7:802. doi: 10.3389/fnhum.2013.00802.
25. Chen L, Chen Y, Zheng H, Zhang B, Wang F, Fang J, et al. Changes in the topological organization of the default mode network in autism spectrum disorder. Brain Imaging and Behavior. 2021;15(2):1058-67. doi: 10.1007/s11682-020-00312-8.
26. Khan S, Gramfort A, Shetty NR, Kitzbichler MG, Ganesan S, Moran JM, et al. Local and long-range functional connectivity is reduced in concert in autism spectrum disorders. Proc Natl Acad Sci U S A. 2013;110(8):3107-12. Epub 2013/01/16. doi: 10.1073/pnas.1214533110. PubMed Central PMCID: PMC3581984.
27. Stoodley CJ, D'Mello AM, Ellegood J, Jakkamsetti V, Liu P, Nebel MB, et al. Altered cerebellar connectivity in autism and cerebellar-mediated rescue of autism-related behaviors in mice. Nat Neurosci. 2017;20(12):1744-51. Epub 2017/12/01. doi: 10.1038/s41593-017-0004-1. PubMed PMID: 29184200; PubMed Central PMCID: PMCPMC5867894.
28. Hong SJ, Vos de Wael R, Bethlehem RAI, Lariviere S, Paquola C, Valk SL, et al. Atypical functional connectome hierarchy in autism. Nat Commun. 2019;10(1):1022. Epub

2019/03/06. doi: 10.1038/s41467-019-08944-1. PubMed PMID: 30833582; PubMed Central PMCID: PMCPMC6399265.

29. Buch AM, Vértes PE, Seidlitz J, Kim SH, Grosenick L, Liston C. Molecular and network-level mechanisms explaining individual differences in autism spectrum disorder. Nat Neurosci. 2023;26(4):650-63. Epub 2023/03/10. doi: 10.1038/s41593-023-01259-x. PubMed PMID: 36894656.
30. Haberl MG, Zerbi V, Veltien A, Ginger M, Heerschap A, Frick A. Structural-functional connectivity deficits of neocortical circuits in the Fmr1 (-/y) mouse model of autism. Sci Adv. 2015;1(10):e1500775. Epub 2015/12/25. doi: 10.1126/sciadv.1500775. PubMed Central PMCID: PMC4681325.
31. Gabrielsen TP, Anderson JS, Stephenson KG, Beck J, King JB, Kellems R, et al. Functional MRI connectivity of children with autism and low verbal and cognitive performance. Molecular Autism. 2018;9(1):67. doi: 10.1186/s13229-018-0248-y.
32. Shofty B, Bergmann E, Zur G, Asleh J, Bosak N, Kavushansky A, et al. Autism-associated Nf1 deficiency disrupts corticocortical and corticostriatal functional connectivity in human and mouse. Neurobiol Dis. 2019;130:104479. Epub 2019/05/28. doi: 10.1016/j.nbd.2019.104479. PubMed PMID: 31128207; PubMed Central PMCID: PMCPMC6689441.
33. Zhang Z, Gibson JR, Huber KM. Experience-dependent weakening of callosal synaptic connections in the absence of postsynaptic FMRP. Elife. 2021;10:e71555. Epub 2021/10/08. doi: 10.7554/eLife.71555. PubMed PMID: 34617509; PubMed Central PMCID: PMCPMC8526058.
34. Zerbi V, Pagani M, Markicevic M, Matteoli M, Pozzi D, Fagiolini M, et al. Brain mapping across 16 autism mouse models reveals a spectrum of functional connectivity subtypes. Mol Psychiatry. 2021;26(12):7610-20. Epub 2021/08/13. doi: 10.1038/s41380-021-01245-4. PubMed PMID: 34381171; PubMed Central PMCID: PMCPMC8873017.
35. Awad PN, Zerbi V, Johnson-Venkatesh EM, Damiani F, Pagani M, Markicevic M, et al. CDKL5 sculpts functional callosal connectivity to promote cognitive flexibility. Mol Psychiatry. 2023. Epub 2023/02/04. doi: 10.1038/s41380-023-01962-y. PubMed PMID: 36737483.
36. Jung M, Kosaka H, Saito DN, Ishitobi M, Morita T, Inohara K, et al. Default mode network in young male adults with autism spectrum disorder: relationship with autism spectrum traits. Molecular Autism. 2014;5(1):35. doi: 10.1186/2040-2392-5-35.
37. Padmanabhan A, Lynch CJ, Schaer M, Menon V. The Default Mode Network in Autism. Biol Psychiatry Cogn Neurosci Neuroimaging. 2017;2(6):476-86. Epub 2017/10/17. doi: 10.1016/j.bpsc.2017.04.004. PubMed PMID: 29034353; PubMed Central PMCID: PMCPMC5635856.
38. Kron M, Howell CJ, Adams IT, Ransbottom M, Christian D, Ogier M, et al. Brain activity mapping in Mecp2 mutant mice reveals functional deficits in forebrain circuits, including key nodes in the default mode network, that are reversed with ketamine treatment. J Neurosci. 2012;32(40):13860-72. Epub 2012/10/05. doi: 10.1523/jneurosci.2159-12.2012. PubMed PMID: 23035095; PubMed Central PMCID: PMCPMC3500840.
39. Liska A, Bertero A, Gomolka R, Sabbioni M, Galbusera A, Barsotti N, et al. Homozygous Loss of Autism-Risk Gene CNTNAP2 Results in Reduced Local and Long-Range Prefrontal Functional Connectivity. Cereb Cortex. 2018;28(4):1141-53. Epub 2017/02/12. doi: 10.1093/cercor/bhx022. PubMed PMID: 28184409.
40. Sinha S, McGovern RA, Sheth SA. Deep brain stimulation for severe autism: from pathophysiology to procedure. Neurosurg Focus. 2015;38(6):E3. Epub 2015/06/02. doi: 10.3171/2015.3.Focus1548. PubMed PMID: 26030703.

41. Penton T, Catmur C, Banissy MJ, Bird G, Walsh V. Non-invasive stimulation of the social brain: the methodological challenges. Soc Cogn Affect Neurosci. 2022;17(1):15-25. Epub 2020/08/01. doi: 10.1093/scan/nsaa102. PubMed PMID: 32734295; PubMed Central PMCID: PMCPMC9083106.
42. Yan H, Elkaim LM, Venetucci Gouveia F, Huber JF, Germann J, Loh A, et al. Deep brain stimulation for extreme behaviors associated with autism spectrum disorder converges on a common pathway: a systematic review and connectomic analysis. J Neurosurg. 2022;137:699-708. Epub 2022/01/22. doi: 10.3171/2021.11.Jns21928. PubMed PMID: 35061980.
43. Bazelot M, Bocchio M, Kasugai Y, Fischer D, Dodson PD, Ferraguti F, et al. Hippocampal Theta Input to the Amygdala Shapes Feedforward Inhibition to Gate Heterosynaptic Plasticity. Neuron. 2015;87(6):1290-303. Epub 2015/09/25. doi: 10.1016/j.neuron.2015.08.024. PubMed Central PMCID: PMCPMC4590554.
44. Kremer JR, Mastronarde DN, McIntosh JR. Computer Visualization of Three-Dimensional Image Data Using IMOD. Journal of Structural Biology. 1996;116(1):71-6. doi: https://doi.org/10.1006/jsbi.1996.0013.
45. Marstal K, Berendsen F, Staring M, Klein S, editors. SimpleElastix: A User-Friendly, Multi-lingual Library for Medical Image Registration. 2016 IEEE Conference on Computer Vision and Pattern Recognition Workshops (CVPRW); 2016 26 June-1 July 2016.
46. Berg S, Kutra D, Kroeger T, Straehle CN, Kausler BX, Haubold C, et al. ilastik: interactive machine learning for (bio)image analysis. Nature Methods. 2019;16(12):1226-32. doi: 10.1038/s41592-019-0582-9.
47. DeNardo LA, Liu CD, Allen WE, Adams EL, Friedmann D, Fu L, et al. Temporal evolution of cortical ensembles promoting remote memory retrieval. Nature Neuroscience. 2019;22(3):460-9. doi: 10.1038/s41593-018-0318-7.

989 # Figures and figure legends

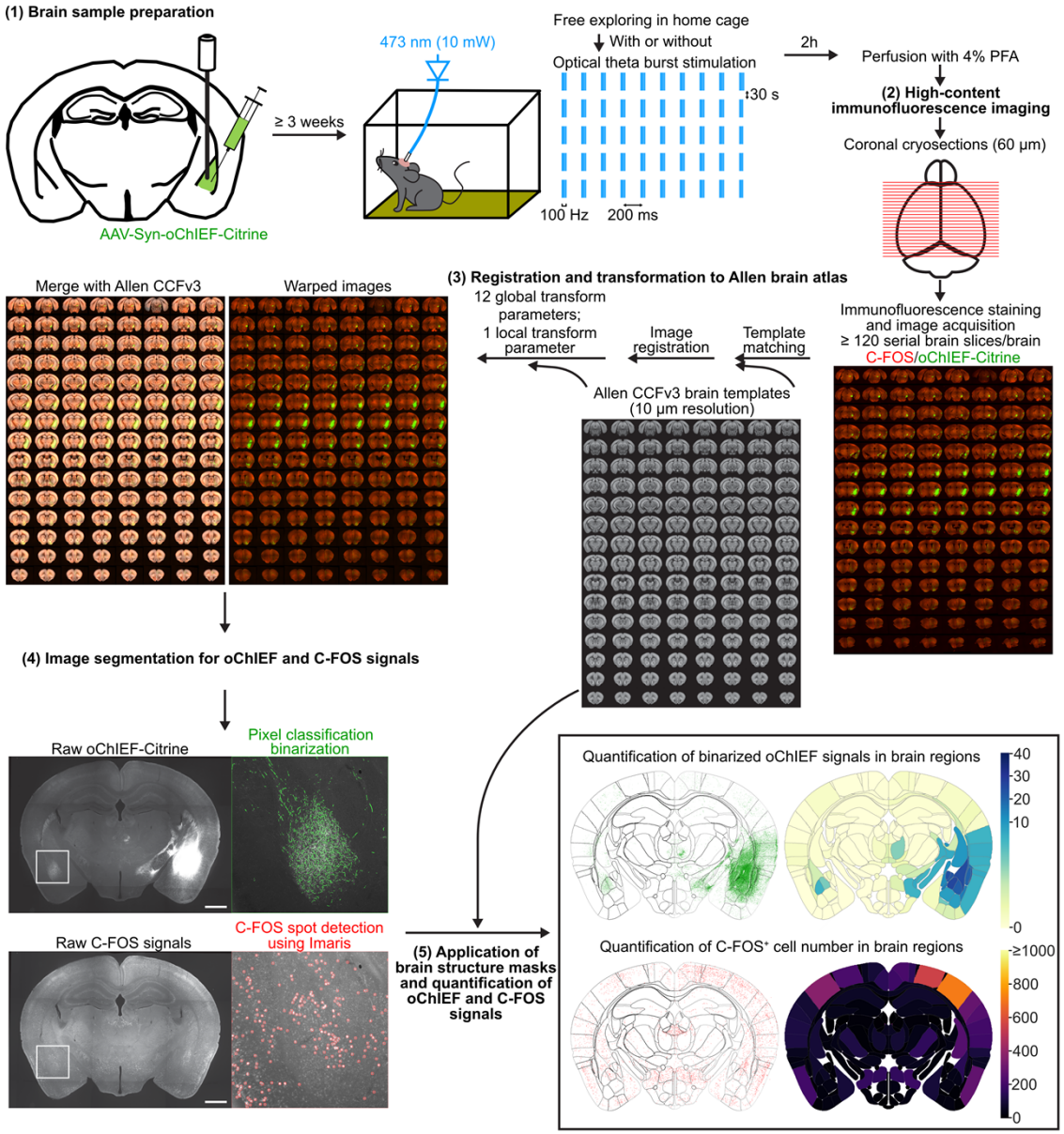

990

991 **Figure 1. Workflow of whole-brain-scale analysis of BLA-derived circuits.** There are five
992 steps in the analysis pipeline. Step 1: Brain sample preparation, involving unilateral BLA
993 infection of oChIEF-Citrine-expressing AAV, *in vivo* theta-burst stimulation (TBS) of the
994 AAV-infected BLA while the awake mice are in their home cage, and brain fixation by PFA 2
995 hours after optogenetic stimulation. Step 2: High-content immunofluorescence imaging. At
996 least 120 coronal cryosections (60 μm/section) of a single mouse brain were subjected to
997 immunostaining to reveal C-FOS^{+} cells and oChIEF-Citrine signals, and then imaged by a high-
998 content imaging system. Step 3: Registration and transformation to the Allen brain atlas. Raw
999 image series were registered to the templates of Allen common coordinate framework version
1000 3 (CCFv3) by sequentially applying 12 global and 1 local transform parameters. Step 4: Image

1001 segmentation for oChIEF and C-FOS signals. The oChIEF signals were isolated by pixel
1002 classification and binarized. C-FOS$^+$ cell locations were detected by the spot detection function
1003 of Imaris (also see **Figure S1**). Step 5: Application of brain structure masks and quantification
1004 of oChIEF and C-FOS signals. Examples of choropleth maps show the quantification of
1005 binarized oChIEF signals (% of pixels/slice, upper) and C-FOS$^+$ cell number (number/slice,
1006 lower) of different brain regions in a single coronal section. Scale bar in Step 4, 1 mm.
1007

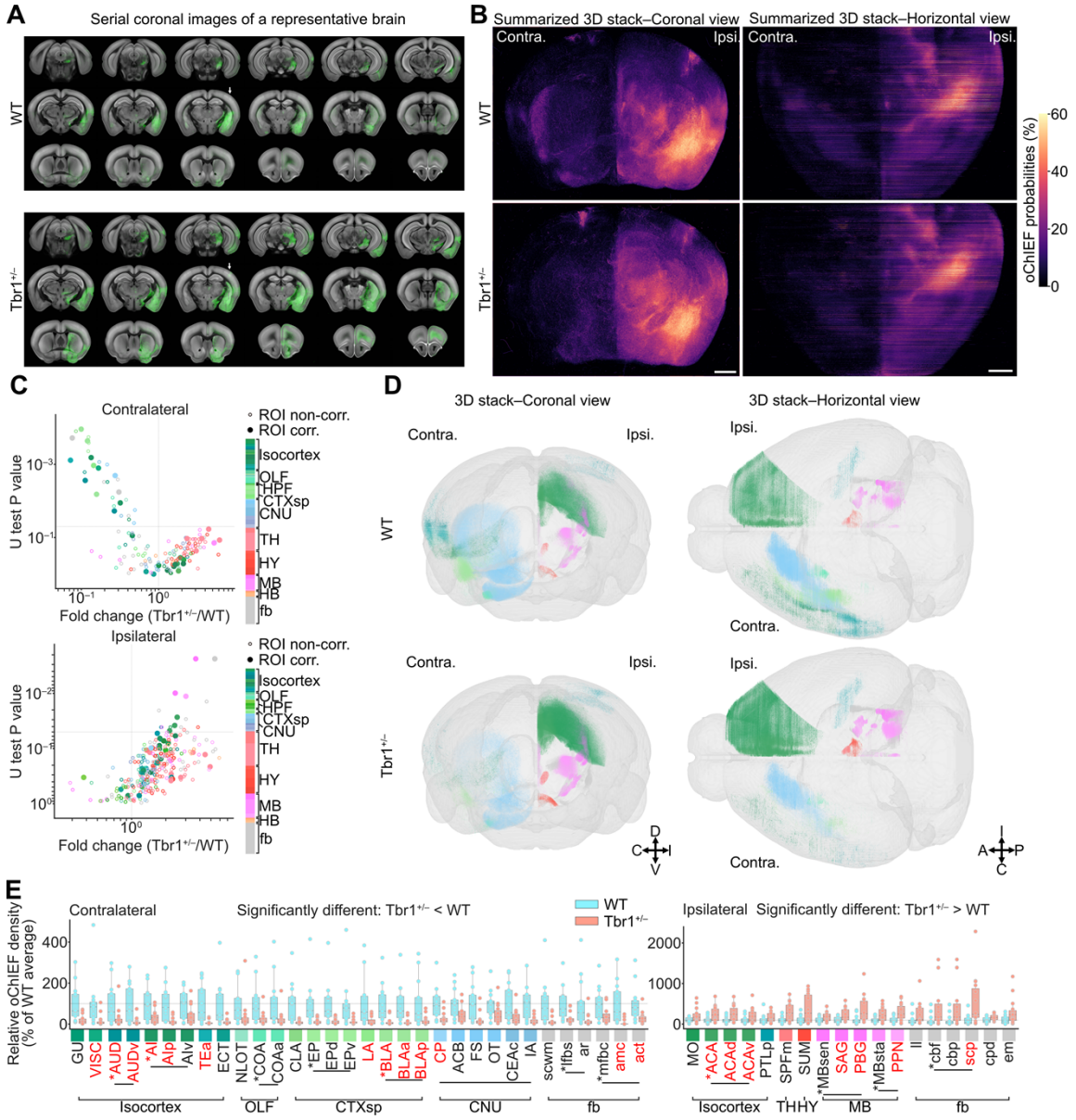

Figure 2. Rewiring of BLA-derived circuits.

(A) Coronal image series of binarized oChIEF-Citrine signals (green) superimposed on a CCFv3 template (gray) of wild-type (WT, upper) and *Tbr1*$^{+/-}$ mouse brain (lower) (also see **Video S1**).

(B) Coronal (left) and horizontal (right) views of summarized 3D stacks with binarized and binned (10 μm^3) oChIEF signals from WT (upper) and *Tbr1*$^{+/-}$ (lower) mouse brains. Color map indicates different probabilities of oChIEF signal in a 10 μm^3 cube (also see **Video S2**).

(C) Structure-wise comparison of binarized oChIEF signals between wild-type and *Tbr1*$^{+/-}$ mouse brains after volume-based quantification (also see **Table S1**). Scatterplots showing the fold-change (*Tbr1*$^{+/-}$/WT) versus significance (Mann-Whitney U test *P* value) of each contralateral (upper) and ipsilateral (lower) brain region are presented. Vertical and horizontal

1020 dotted lines represent fold change = 1 and U test *P* value = 0.05, respectively. Colors represent
1021 brain region identities. Open and filled circles represent ROI non-corrected and corrected brain
1022 regions, respectively.
1023 (D) Coronal (left) and horizontal (right) views of 3D stacks with binarized and binned (10 μm^3)
1024 oChIEF pixels in the brain regions displaying significantly different BLA-circuit rewiring
1025 (P<0.05) between wild-type (upper) and *Tbr1*$^{+/-}$ mice (lower). Colors represent brain regions
1026 as shown in (C). Alpha levels (0–1) of the brain region color represent scaled oChIEF
1027 probabilities.
1028 (E) Box plots showing comparisons of relative oChIEF signal density between WT and *Tbr1*$^{+/-}$
1029 mouse brains. Only the regions displaying a significant difference (P <0.05) are shown. Left,
1030 contralateral; right, ipsilateral. Boxes show median and interquartile ranges, and whiskers
1031 extend to the rest of the distribution except for outliers. Spots represent individual samples.
1032 Asterisks label the parental brain regions of subsequent offspring regions grouped by the
1033 horizontal lines. Red font indicates ROI-corrected regions. Color bars under the charts represent
1034 brain region identities, as shown in (C). The horizontal dotted lines represent the WT average,
1035 i.e., 100%.
1036 Scale bar in (B), 1 mm. Sample sizes of mice are the same for (B)-(E) (WT, n=13; *Tbr1*$^{+/-}$, n=
1037 15).
1038

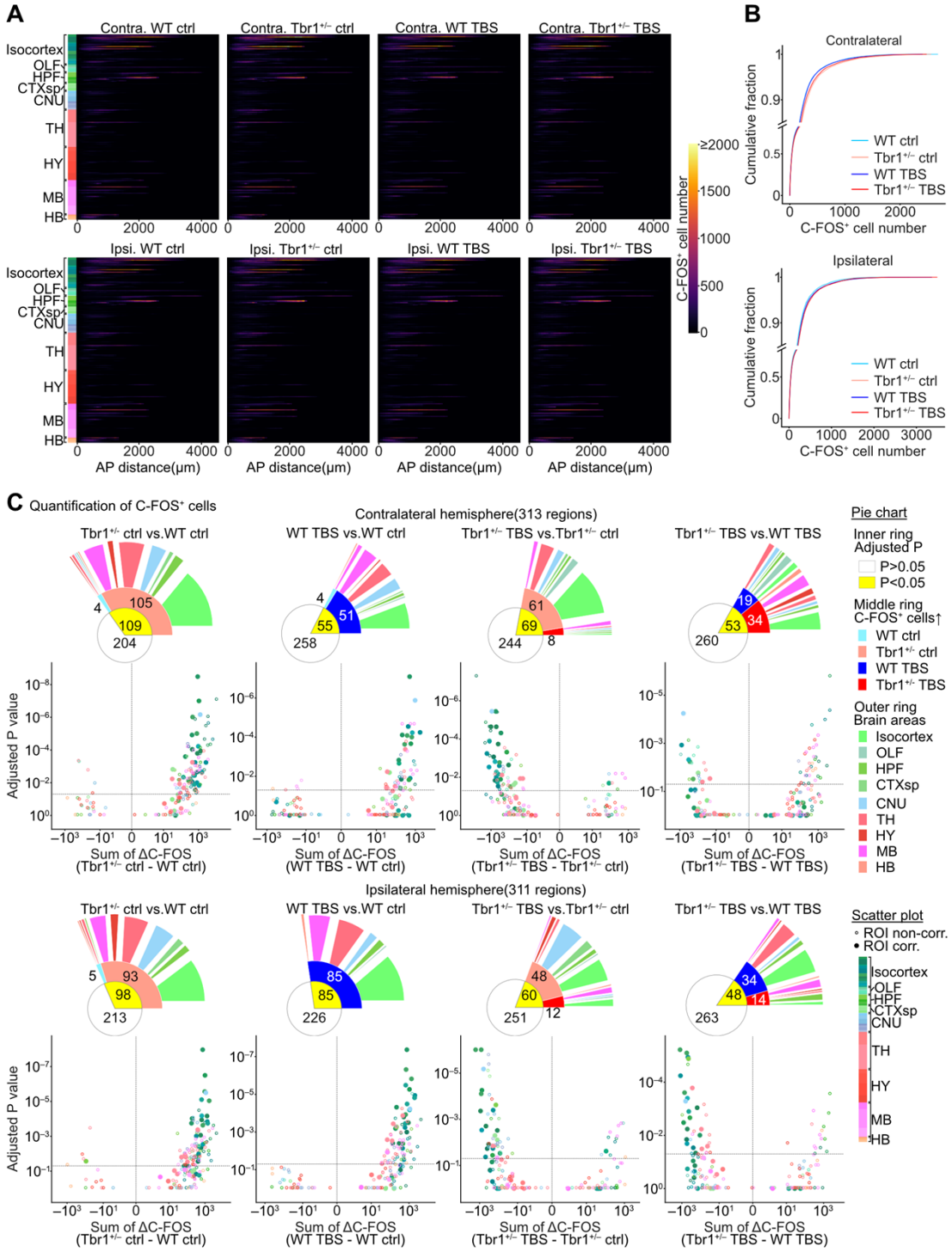

Figure 3. Differential C-FOS expression in WT and *Tbr1*$^{+/-}$ mouse brains with or without activation of BLA-derived circuits.

(A) Slice-based quantification of C-FOS^{+} cell distributions in WT ctrl, *Tbr1*$^{+/-}$ ctrl, WT TBS and *Tbr1*$^{+/-}$ TBS groups (left to right). Heatmaps show binned (100 μm) and averaged C-FOS^{+} cell numbers along the anterior-poster axis (AP distance, rows) of every brain region (columns) in the contralateral (Contra., upper panel) and ipsilateral (Ipsi., lower panel) hemispheres.

1046 (B) Cumulative plots of the numbers of C-FOS^{+} cells along the AP for all brain regions in the
1047 four experimental groups (WT ctrl, *Tbr1*$^{+/-}$ ctrl, WT TBS and *Tbr1*$^{+/-}$ TBS).
1048 (C) Structure-wise comparison of C-FOS^{+} cell numbers in the contralateral (upper) and
1049 ipsilateral (lower) brain hemispheres of the four pairwise-compared groups (left to right, *Tbr1*$^{+/-}$
1050 ctrl vs. WT ctrl, WT TBS vs. WT ctrl, *Tbr1*$^{+/-}$ TBS vs. *Tbr1*$^{+/-}$ ctrl, *Tbr1*$^{+/-}$ TBS vs. WT TBS).
1051 Each scatterplot shows the summed C-FOS^{+} cell number difference along the AP axis (Sum of
1052 ΔC-FOS) versus statistical significance (Adjusted *P* value) for each brain region of the
1053 pairwise-compared groups (also see **Table S2, Figure S7b**). Friedman one-way repeated
1054 measure analyses, followed by post-hoc pairwise tests with Bonferroni correction, were used
1055 for statistical analysis. Vertical and horizontal dotted lines represent the Sum of ΔC-FOS=0 and
1056 Adjusted *P* value=0.05, respectively. Colors represent brain region identities. Open and filled
1057 circles represent ROI-non-corrected and -corrected brain regions, respectively. Each pie chart
1058 above the scatterplot illustrates the proportions of brain regions that fit each condition annotated
1059 in the right panel.
1060 Sample sizes of mouse numbers are identical in (A)-(C) (WT ctrl, n=6; *Tbr1*$^{+/-}$ ctrl, n=7; WT
1061 TBS, n=7; *Tbr1*$^{+/-}$ TBS, n=7).
1062

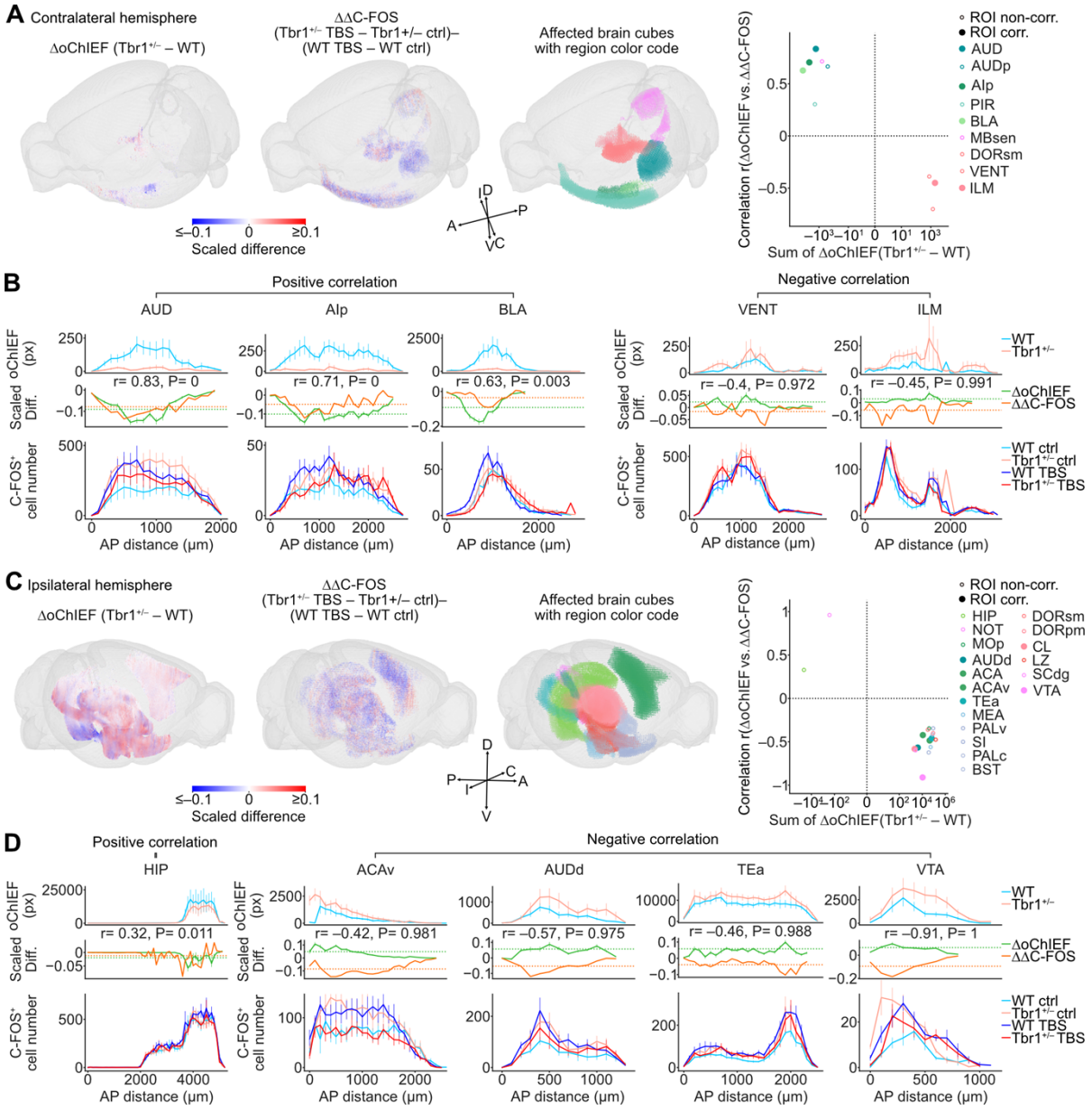

Figure 4. Correlations of BLA axonal projection patterns and C-FOS expression of *Tbr1*$^{+/-}$ mice.

(A) 3D maps of rewired BLA-derived circuits (left, 10 μm^3 binned cubes with binarized oChIEF signals) and differentially TBS-derived C-FOS expression levels (middle, 100 μm^3 binned C-FOS$^+$ cell numbers) in affected brain regions (right) with the Allen brain region color code. Only the results of contralateral hemisphere are shown herer. Color maps of the scaled difference show the differential oChIEF signal probabilities (left 3D map, ΔoChIEF of *Tbr1*$^{+/-}$ – WT) and the difference between the C-FOS modulatory effects of BLA-derived circuits in *Tbr1*$^{+/-}$ (ΔC-FOS of *Tbr1*$^{+/-}$ TBS – *Tbr1*$^{+/-}$ ctrl) and WT (ΔC-FOS of WT TBS – WT ctrl) mouse brains (middle left 3D map, ΔΔC-FOS). Scatterplots on the right panels show the sum of ΔoChIEF (*Tbr1*$^{+/-}$ – WT) versus the correlation between ΔoChIEF and ΔΔC-FOS for the

1075 brain regions of contralateral hemispheres. Colors indicate brain region identities. Open and
1076 filled circles represent ROI-non-corrected and -corrected brain regions, respectively.
1077 (B) Examples of brain regions that have positive or negative correlations between rewired BLA-
1078 derived circuits of *Tbr1*$^{+/-}$ mice and differential TBS-derived C-FOS expression levels. The
1079 oChIEF distributions (WT and *Tbr1*$^{+/-}$, upper panel), C-FOS^{+} cell distributions (WT ctrl,
1080 *Tbr1*$^{+/-}$ ctrl, WT TBS and *Tbr1*$^{+/-}$ TBS, lower panel), and scaled differences (ΔoChIEF and
1081 ΔΔC-FOS, middle panel) along the AP axis are shown. Dashed lines in scaled differences plots
1082 represent the average 99th percentile of scaled differences calculated from the pair-subtraction
1083 population data with 1000 times AP axis reshuffling.
1084 (C) The 3D maps of the results of ipsilateral hemisphere.
1085 (D) The correlation between oChIEF and C-FOS signals at the ipsilateral hemisphere.
1086 Data represent mean ± SEM. Contralateral (A)-(B) and ipsilateral (C)-(D) hemispheres were
1087 analyzed separately. Sample sizes were the same in (A)-(D) (oChIEF data: WT, n=13; *Tbr1*$^{+/-}$,
1088 n= 14. C-FOS data: WT ctrl, n=6; *Tbr1*$^{+/-}$ ctrl, n=7; WT TBS, n=7; *Tbr1*$^{+/-}$ TBS, n=7).
1089

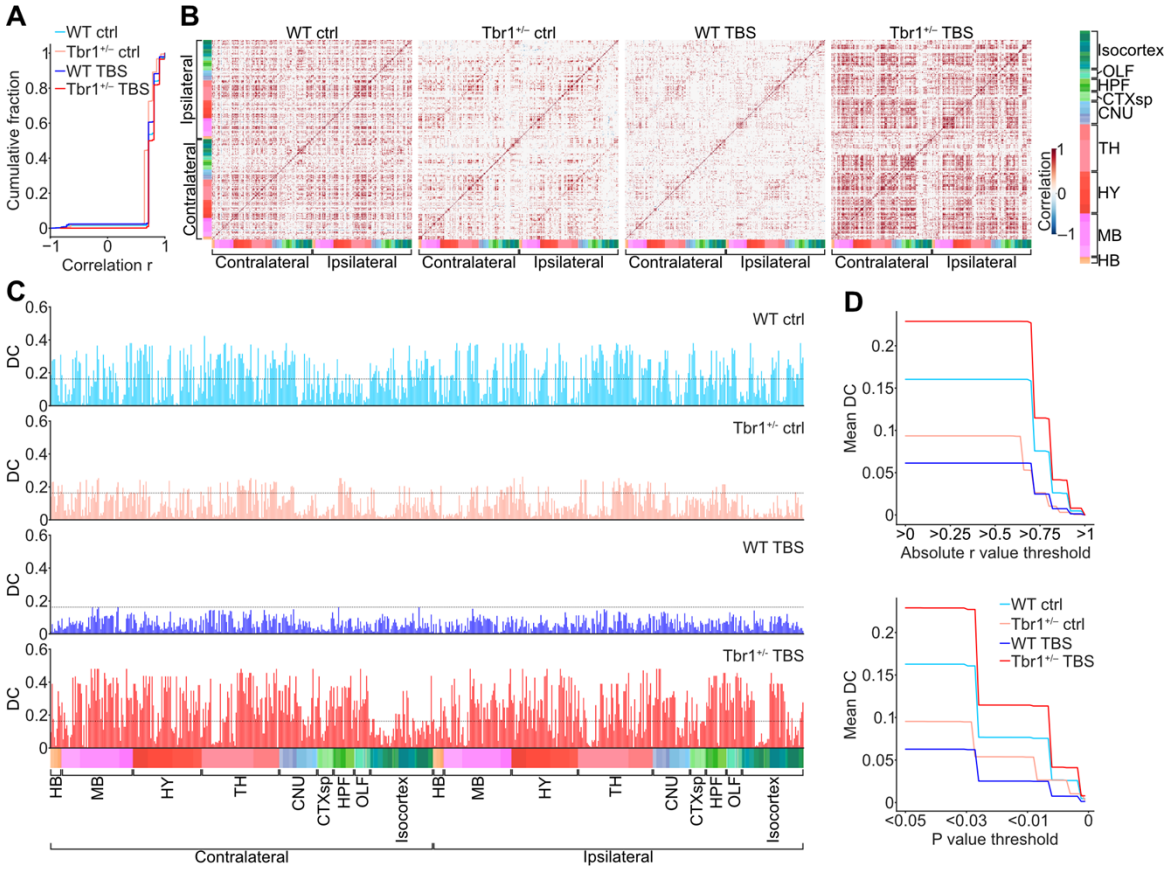

Figure 5. Distinct inter-regional correlations of C-FOS expression in WT and *Tbr1*$^{+/-}$ mouse brains with or without BLA-derived activation.

(A) Cumulative plot showing the probability of all significant inter-regional correlations ($P < 0.05$, Kendall's rank correlation) of C-FOS expression levels for the four experimental groups.

(B) Matrices showing whole-brain inter-regional correlations of C-FOS expression in the WT ctrl, *Tbr1*$^{+/-}$ ctrl, WT TBS and *Tbr1*$^{+/-}$ TBS groups (left to right).

(C) Plots showing Degree Centrality (DC, y-axis) of each brain region (annotated in the bottom row, x-axis).

(D) Plots showing mean DC of networks (y-axis) with different thresholds for the correlation coefficient r (x-axis, upper panel) or correlation *P* values (x-axis, lower panel).

Brain regions are annotated with color codes in (B)-(C). The sample sizes of mice are the same in (A)-(D) (WT ctrl, n=7; *Tbr1*$^{+/-}$ ctrl, n=8, WT TBS, n=7; *Tbr1*$^{+/-}$ TBS, n=7).

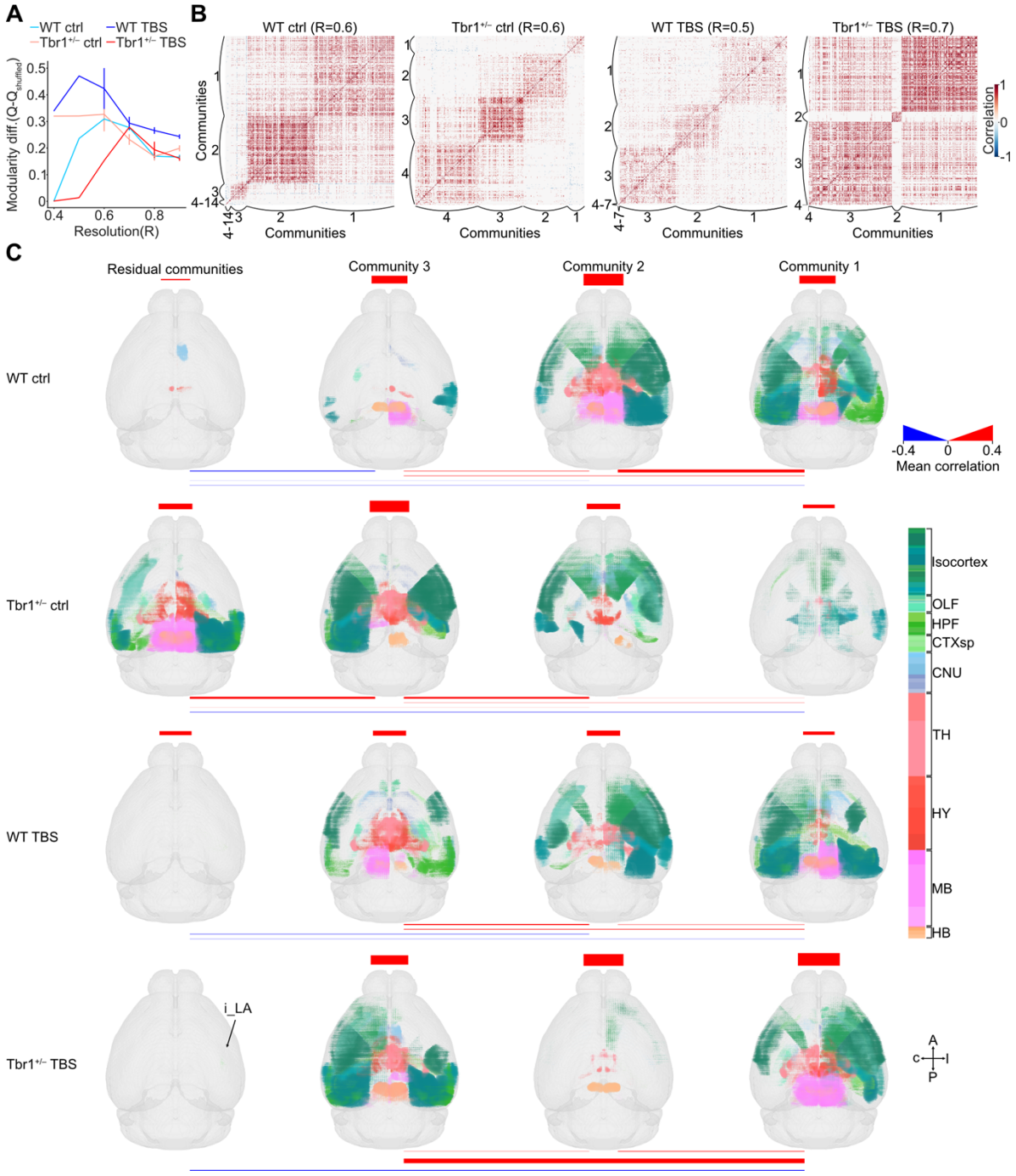

Figure 6. Modular organization of C-FOS expression correlation networks.

(A) Plot showing the differences in modularity (y-axis) between real networks (Q) and shuffled networks ($Q_{shuffled}$) when a different resolution parameter R (x-axis) was used for community detection in the four experimental groups.

(B) The same datasets of inter-regional correlations for C-FOS expression are shown in **Figure 5B**, except the inter-regional pair positions were sorted by their communities. The R values that generate the maximum difference in Q between real and shuffled networks for each experimental group are indicated and they were used to analyze network communities.

1113 (C) 3D maps of binned and averaged C-FOS$^+$ cubes for each community (rows) of the four
1114 experimental groups (columns). C-FOS$^+$ cubes are shown in brain region color codes, with their
1115 sizes representing the relative normalized density of C-FOS$^+$ cells within binned cubes (100
1116 μm^3) (also see **Figure S7D**). Mean correlations within (the bars at the top of 3D maps) and
1117 between communities (the lines under the 3D maps) are annotated according to differential
1118 extents (thickness) and polarity (color). Thicker bars or lines represent a higher degree of
1119 correlation, whether positive (red) or negative (blue). Sample sizes are the same as in **Figure**
1120 **5.**
1121

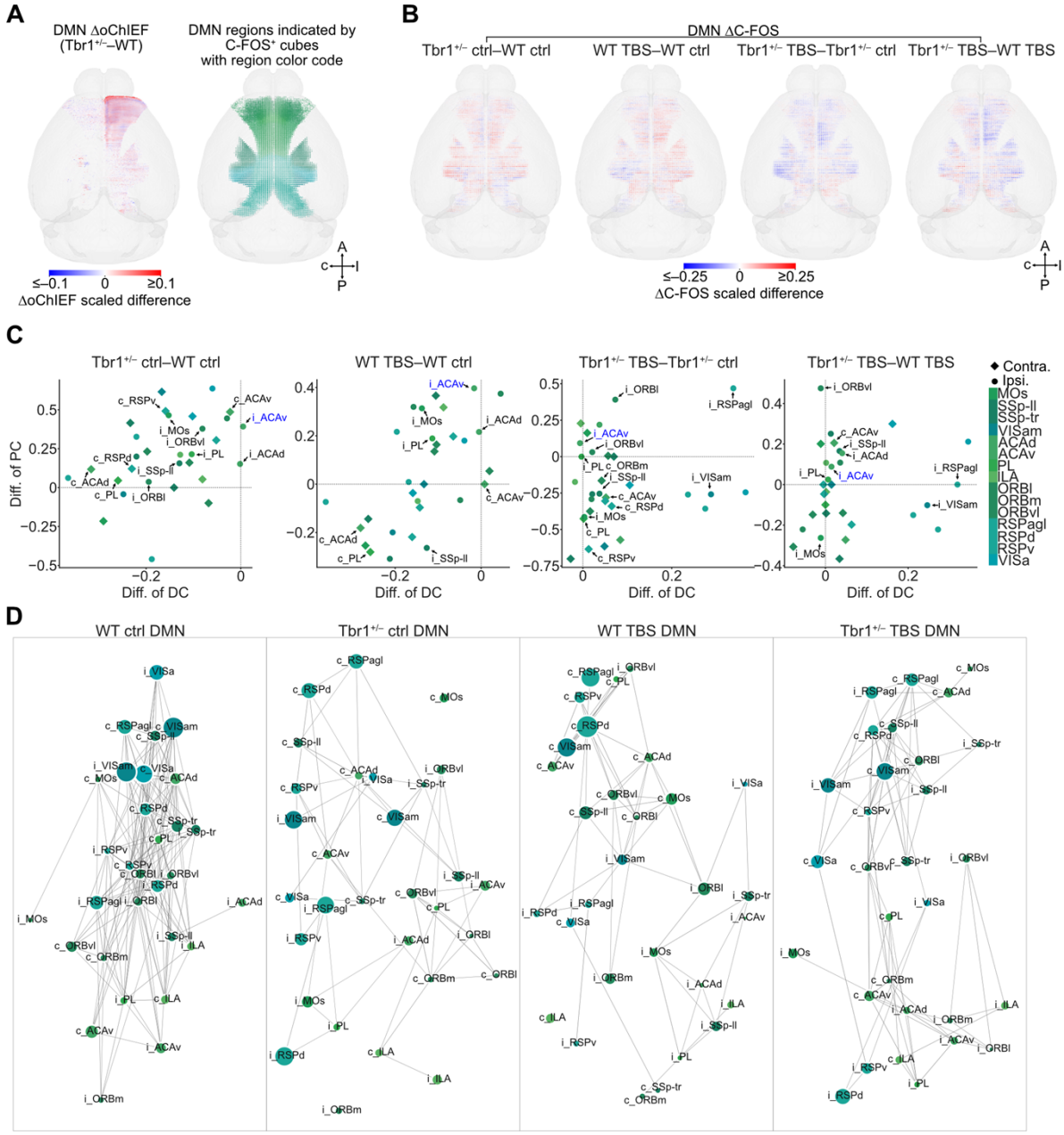

Figure 7. Comparison of default mode networks (DMN) in WT ctrl, *Tbr1*$^{+/–}$ ctrl, WT TBS and *Tbr1*$^{+/–}$ TBS groups.

(A) The differences of BLA axonal projections into DMN regions for *Tbr1*$^{+/–}$ and WT mice, as revealed by ΔoChIEF for 10 μm^3 binned cubes.

(B) 3D maps showing differences in density of C-FOS$^+$ cells (ΔC-FOS, 100 μm^3 bins) for the DMN of experimental group pairs. The heat maps indicate the scaled differences for ΔoChIEF (A) and ΔC-FOS (B).

(C) Structure-wise comparison of DMN properties for four experimental group pairs. Each scatterplot shows the difference in DC versus the difference in participation coefficient (PC) in each DMN brain region for each group pair.

1133 (D) Visualization in spring layout of the DMN networks for the four experimental groups. Brain
1134 regions (nodes) having many reciprocal C-FOS correlations (edges) are closer together.
1135 The color of each node represents brain region identity. The size of the node represents the
1136 normalized C-FOS density of the brain region. Labels "i_" and "c_" represent ipsilateral or
1137 contralateral brain regions, respectively. DMN region color codes are identical for (A), (C) and
1138 (D). In (C), DMN regions labeled in black indicate regions showing a significant difference in
1139 C-FOS^{+} cell numbers between pairwise-compared groups. Blue-labeled i_ACAv exhibited a
1140 negative correlation between the amount of BLA-derived axonal innervations and its
1141 modulatory effects on C-FOS expression patterns. Thus, the i_ACAv received enhanced BLA
1142 axonal projections that induce net inhibitory effects on neuronal activities in the *Tbr1*$^{+/-}$ mouse
1143 brain. All DMN regions are ROI-corrected. Sample sizes for the DMN network analysis are
1144 identical to those described in **Figure 5A, 5B**. Sample sizes for the DMN ΔC-FOS and DMN
1145 ΔoChIEF analyses are the same as those described in **Figure 4**.
1146

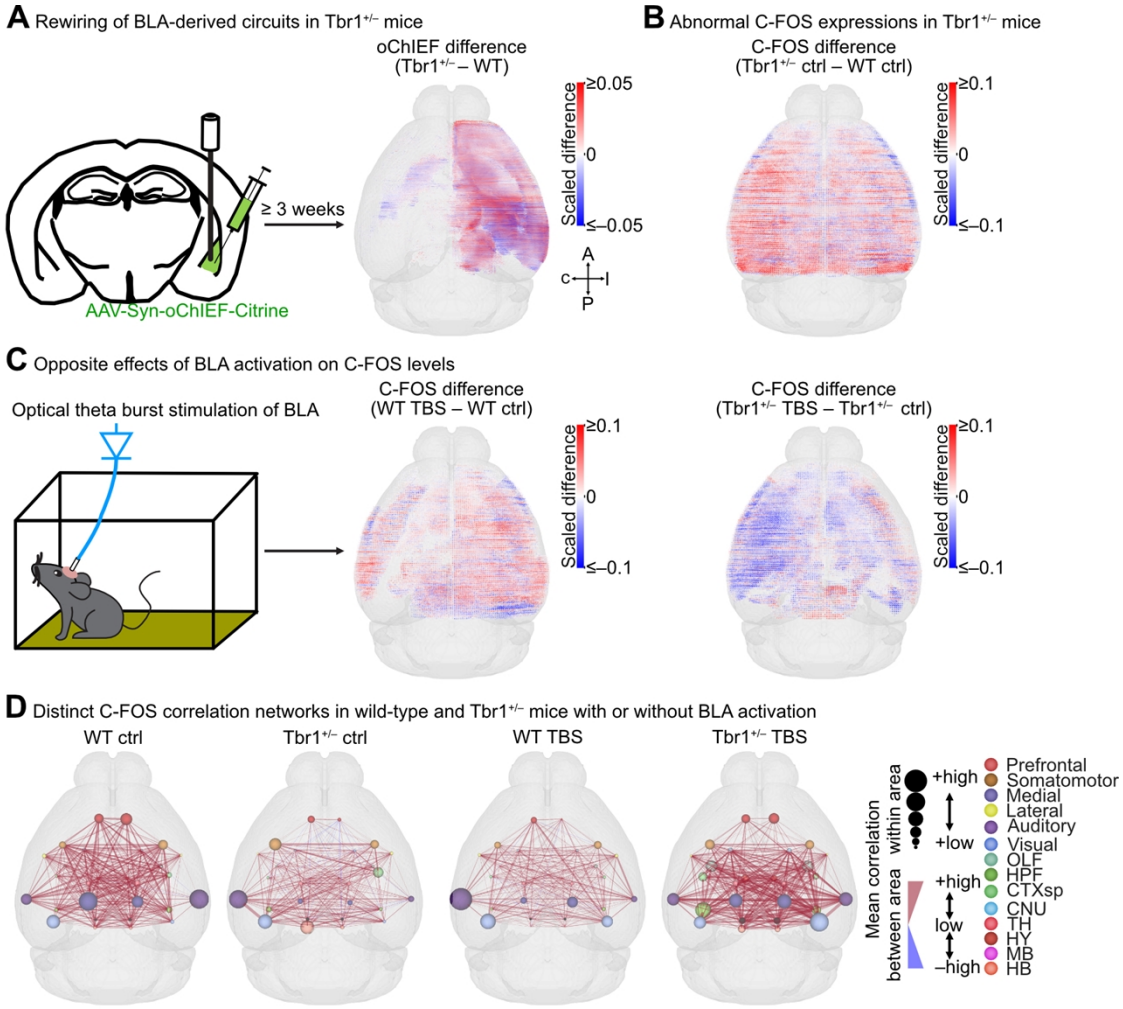

Figure 8. Whole-brain alteration of the amygdalar mesoscopic connectome and synchronization in the *Tbr1*$^{+/–}$ mouse brain.

(A) Differences in the amygdalar mesoscopic connectome between wild-type and Tbr1$^{+/–}$ mice are revealed by oChIEF-Citrine expression in a unilateral BLA. *Tbr1*$^{+/–}$ mice massively lose contralateral axonal projections of the BLA and exhibit mistargeting of ipsilateral BLA axons.

(B) The global neuronal activities revealed by C-FOS expression are different between wild-type and *Tbr1*$^{+/–}$ mice. In general, *Tbr1*$^{+/–}$ mice exhibit higher C-FOS expression during wakefulness.

(C) BLA activation elicits opposing effects on C-FOS levels when comparing wild-type to *Tbr1*$^{+/–}$ mice. In general, BLA activation potentiates C-FOS levels in wild-type mice, whereas it reduces C-FOS expression in *Tbr1*$^{+/–}$ mice.

(D) The neuronal synchronization patterns revealed by C-FOS correlation networks differ between wild-type and *Tbr1*$^{+/–}$ mice and are differentially modulated by BLA activation. Neuronal activities are generally less synchronized in the *Tbr1*$^{+/–}$ mouse brain. However, after BLA activation, neuronal synchronization is reduced in wild-type mice but increased in *Tbr1*$^{+/–}$

1163 mice. The C-FOS correlation networks shown here are simplified in that brain regions
1164 belonging to the same primary brain areas (colored spots) have been combined. Mean
1165 correlations within and between primary brain areas were calculated and are expressed as spot
1166 size and edge thickness, respectively.
1167

Supporting Information

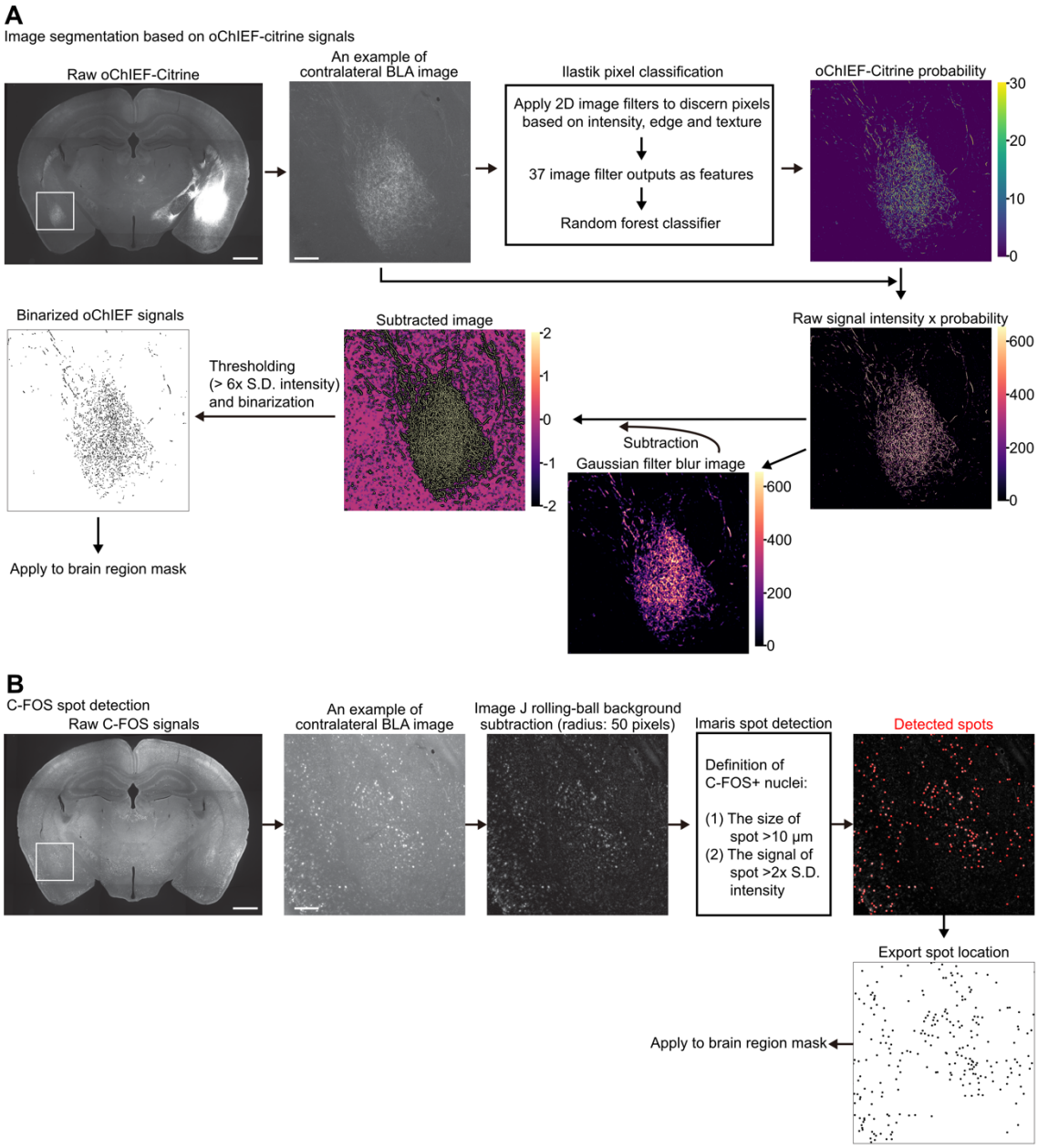

Figure S1. Workflow for image segmentation of oChIEF and C-FOS signals. (A) oChIEF signal segmentation. Raw images of oChIEF-Citrine signals were subjected to an ilastik pixel classification algorithm to obtain the oChIEF signal probability map. Filtered images were created by applying the oChIEF signal probability map to the raw images. Subtracted images were created by subtracting the filtered image from a Gaussian filter blurred version of the same image. Finally, the subtracted image was subjected to thresholding and binarization to get binarized oChIEF signals.

1178 (B) Detection of C-FOS^{+} nuclei. Raw images of C-FOS signals were subjected to rolling-ball
1179 background subtraction and then the Imaris spot detection algorithm was used to detect C-FOS
1180 spot signals. Spot locations were then exported for quantification.
1181

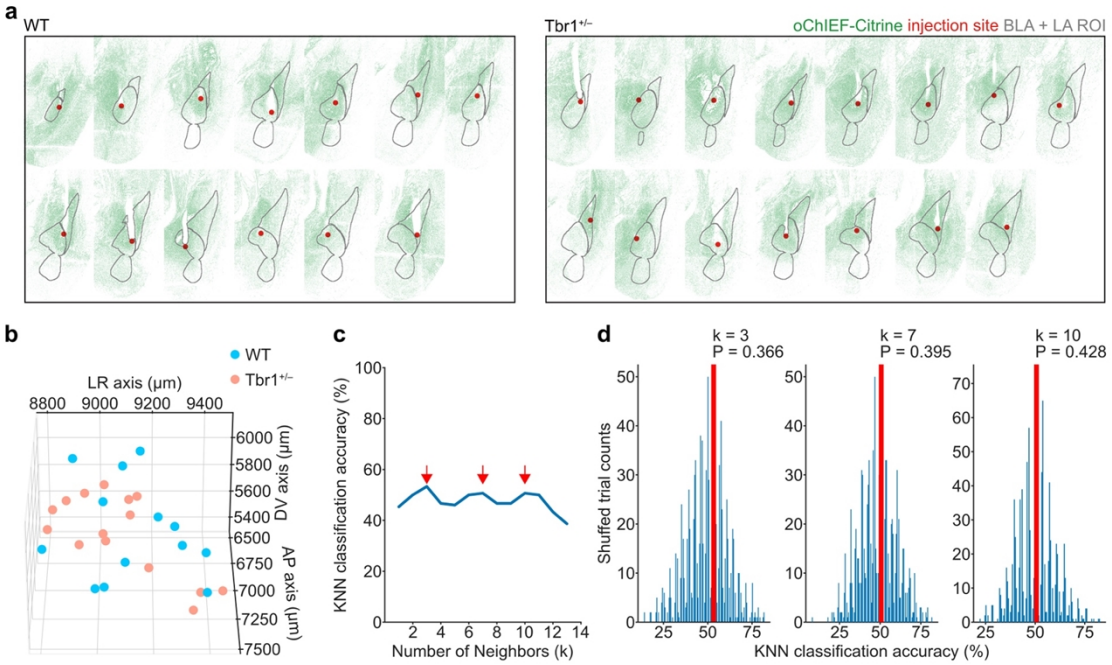

Figure S2. Spatial distribution of oChIEF-Citrine-expressing AAV injection sites in wild-type and *Tbr1*$^{+/-}$ mouse brains.

(A) Images showing oChIEF-Citrine expression (green) in the AAV injection sites (red spots) of wild-type (left panels) and *Tbr1*$^{+/-}$ (right panels) mouse brains. BLA and LA regions are outlined.

(B) Distribution of virus injection sites in CCFv3 space.

(C) Differentiation of virus injection site locations between wild-type and *Tbr1*$^{+/-}$ mouse brains by k-nearest neighbors (KNN) algorithm-based classification. Plot showing the parameter number of KNN neighbors (k) versus KNN classification accuracies.

(D) Three k parameters that presented relatively high classification accuracy (arrows in (C)) were used to compare (wild-type versus *Tbr1*$^{+/-}$) the real classification accuracy (indicated by the red line) with the classification accuracy distributions of virus injection locations shuffled 1000-times. The results support that the spatial distributions of injection sites are indistinguishable between wild-type and *Tbr1*$^{+/-}$ mice.

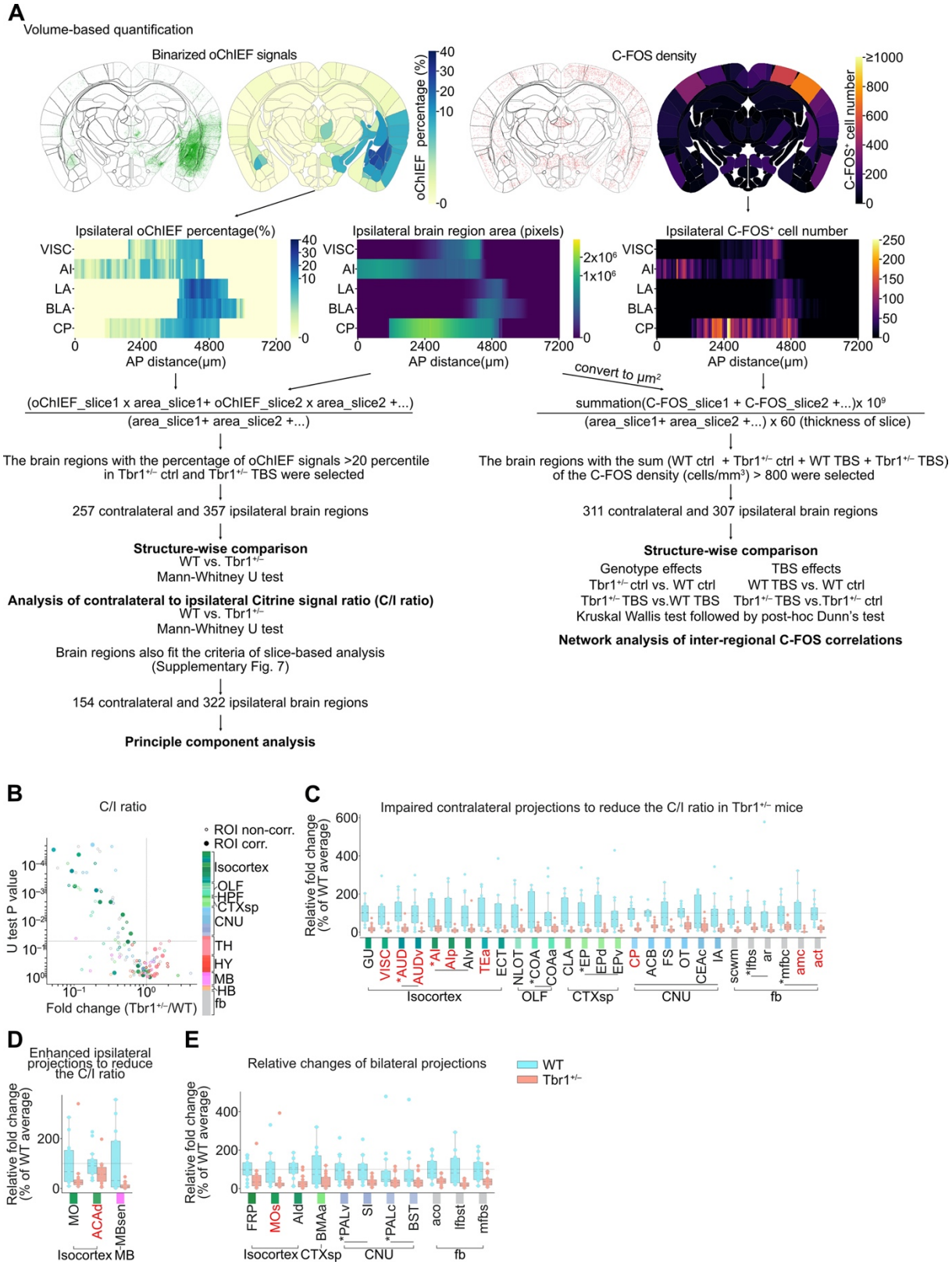

Figure S3. Volume-based quantification and rewiring of bilateral BLA axon projections in *Tbr1*$^{+/-}$ mouse brain.

(A) Binarized oChIEF-Citrine percentage and C-FOS cell density in each brain region volume were calculated and compared between experimental groups.

1204 (B)-(E) Bilateral BLA axon projections to the same regions of both brain hemispheres were
1205 investigated by determining the ratio of contralateral Citrine signal to ipsilateral Citrine signal
1206 (the C/I ratio) for each brain region.
1207 (A) Scatterplot showing the fold-change (Tbr1$^{+/-}$/WT) in C/I ratio versus significance (Mann-
1208 Whitney U test *P* value) in each brain region receiving bilateral BLA axon projections in wild-
1209 type mouse brains. Vertical and horizontal dotted lines represent fold change = 1 and U test *P*
1210 value = 0.05, respectively. Colors represent brain region identities. Open and filled circles
1211 represent ROI-non-corrected and -corrected brain regions, respectively.
1212 (B)-(D) Box plots showing comparisons of the relative fold-change in C/I ratio among brain
1213 regions displaying significantly different C/I ratios ($P<0.05$) between WT and *Tbr1*$^{+/-}$ mouse
1214 brains. Brain regions were further categorized into the three groups shown in (B)-(D), based on
1215 the cause of differential C/I ratios: (B) brain regions exhibiting impaired contralateral BLA
1216 axon projections; (C) brain regions showing significantly enhanced ipsilateral BLA axon
1217 projections in *Tbr1*$^{+/-}$ mouse brains; (D) brain regions exhibiting a relative change in bilateral
1218 projection. The regions shown in (B) and (C) are also present in **Figure 2C-2E**, whereas those
1219 in (D) are not.
1220 In the box plots, boxes show median and interquartile range and whiskers extend to show the
1221 rest of the distribution except for outliers. Spots represent individual samples. Asterisks label
1222 parental brain regions of the following offspring regions, bounded by horizontal lines. Regions
1223 in red font were ROI-corrected. Colored bars under the charts represent the brain identities, as
1224 shown in (A). Horizontal dotted lines represent 100% of the relative fold-change of the C/I ratio
1225 compared to the average of the WT group. Sample sizes of mice are the same in (A)-(D) (WT,
1226 n=13; *Tbr1*$^{+/-}$, n= 15).
1227

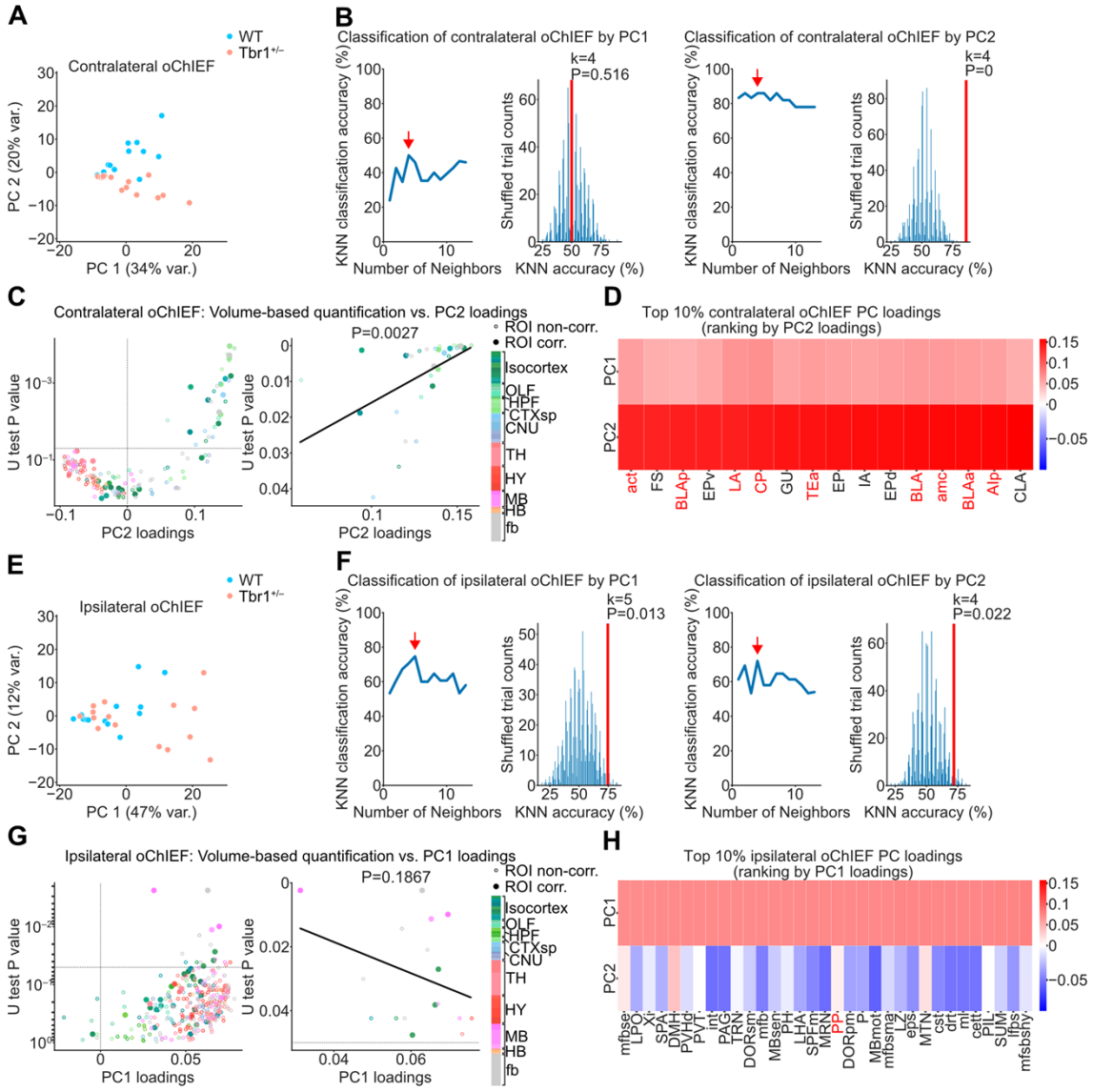

Figure S4. Principal component analysis (PCA) of BLA-derived circuits in wild-type and *Tbr1*$^{+/-}$ mouse brains.

(A)-(H) Data on oChIEF percentages in contralateral (A)-(D) or ipsilateral (E)-(H) brain regions were subjected to PCA and reduced to the first two principal components (PCs).

(A), (E) Plots showing PC locations of individual mouse brain samples projected to the space defined by PC1 (x-axis) and PC2 (y-axis).

(B), (F) Differentiation of PC locations between wild-type and *Tbr1*$^{+/-}$ mouse brains by KNN classification along the PC1 or PC2 axis. For each KNN classification, the left panel shows a parameter series of number of neighbors (k) used for KNN plotted against KNN classification accuracies, and the right panel shows the most appropriate k parameters with relatively high classification accuracy that were used to compare (wild-type versus *Tbr1*$^{+/-}$ data) the real classification accuracy (indicated by the red line) with the classification accuracy distributions of PC locations shuffled 1000-times.

1242 (C), (G) Left panels show PC2 (C) or PC1 (G) loadings versus the significance level (U test *P*
1243 value) of volume-based quantification of oChIEF percentage (data from **Figure 2C**) in each
1244 contralateral (C) or ipsilateral (G) brain region. Right panels show correlations of top 10 PC2
1245 (C) or PC1 (G) loadings with their significance level of volume-based quantification of oChIEF
1246 percentage. (D), Contralateral brain regions with the top 10 PC2 loadings and their
1247 corresponding PC1 loadings. (H), Ipsilateral brain regions with the top 10 PC1 loadings and
1248 their corresponding PC2 loadings. Sample sizes of mice are identical in (A)-(H) (WT, n=13;
1249 *Tbr1*$^{+/-}$, n= 15).
1250

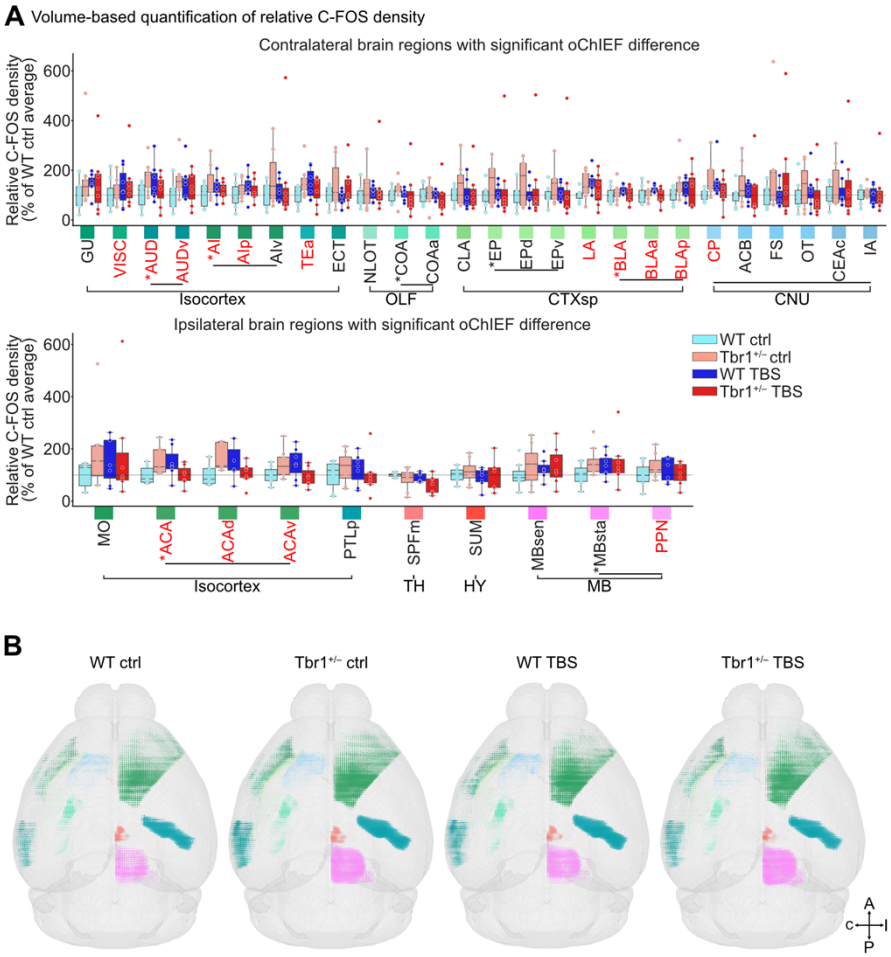

Figure S5. Comparison of C-FOS expression in the affected BLA projection regions between the WT ctrl, *Tbr1*$^{+/-}$ ctrl, WT TBS and *Tbr1*$^{+/-}$ TBS groups.

(A) Volume-based quantification of relative C-FOS density in affected BLA projection regions. Box plots show the comparisons of relative C-FOS density among affected regions for all BLA axonal projections in the contralateral (upper panel) and ipsilateral brain hemispheres (lower panel), except for the regions of white matter. Boxes show median and interquartile range, and whiskers extend to the rest of the distribution except for outliers. Spots represent individual samples. A Kruskal–Wallis test followed by a post-hoc Dunn's test was used for statistical analysis. Asterisks label parental brain regions of the following offspring regions, bounded by horizontal lines. Red font indicates ROI-corrected brain regions. Colored bars under the charts represent brain identities. The horizontal dotted line represents 100% of the relative C-FOS density compared to the average of the WT group.

(B) 3D maps of binned and averaged C-FOS^{+} cubes in affected BLA projection regions for the four experimental groups. The sizes of spots represent the normalized C-FOS densities within binned cubes (100 μm^{3}). Region color codes are as applied in (A)-(B). Sample sizes of mice are identical in (A), (B) (WT ctrl, n=7; *Tbr1*$^{+/-}$ ctrl, n=8; WT TBS, n=7; *Tbr1*$^{+/-}$TBS, n=7).

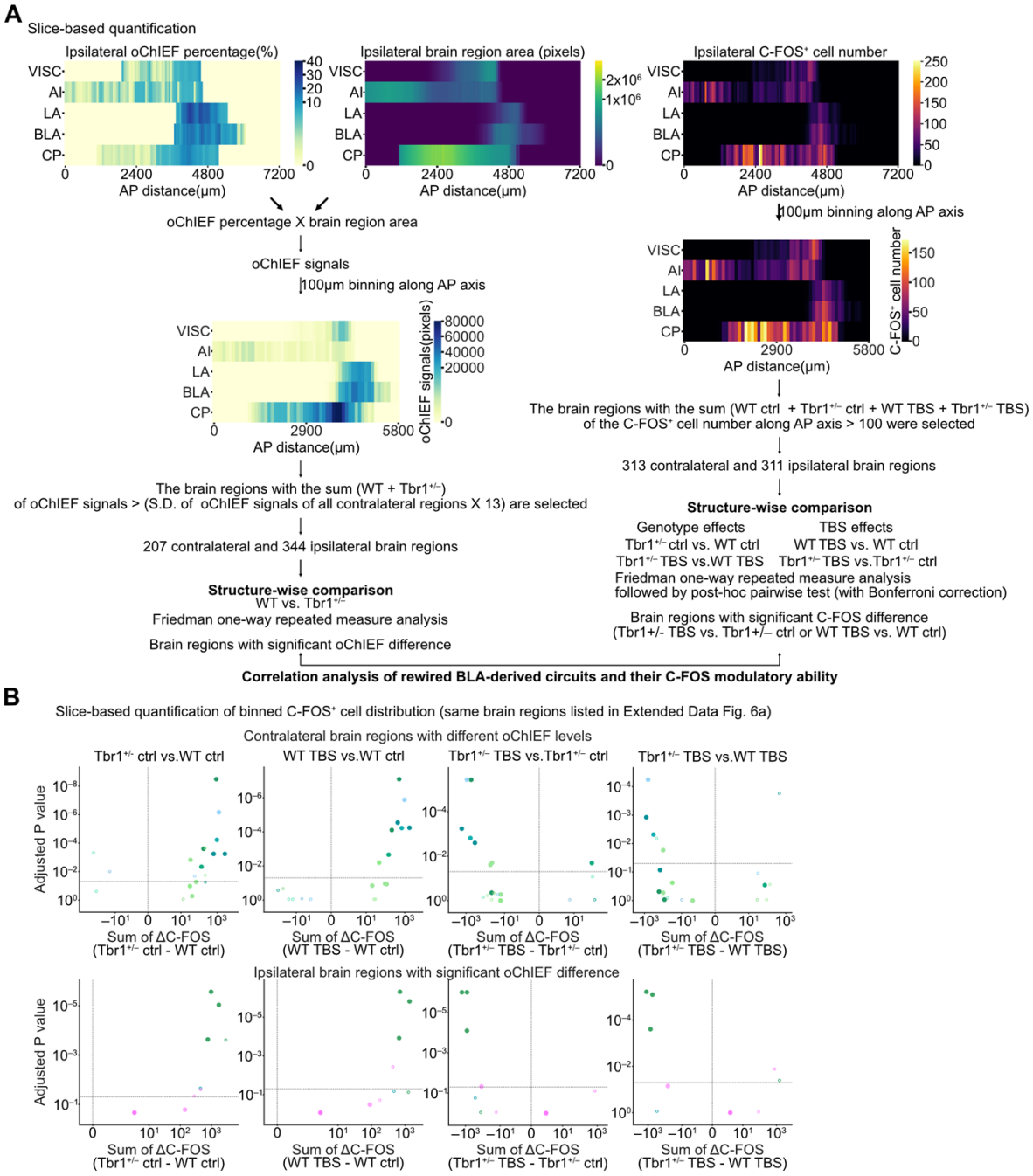

Figure S6. Slice-based quantification of oChIEF and C-FOS signals.

(A) Workflow of slice-based quantification. The pixel distributions of oChIEF and the distributions of C-FOS^{+} cells along the AP axis of each brain region were calculated and compared between experimental groups.

(B) Slice-based quantification of C-FOS expression in affected BLA projection regions for the four pairwise-compared groups (left to right, *Tbr1*$^{+/–}$ ctrl vs. WT ctrl, WT TBS vs. WT ctrl, *Tbr1*$^{+/–}$ TBS vs. *Tbr1*$^{+/–}$ ctrl, *Tbr1*$^{+/–}$ TBS vs. WT TBS). The sample size of each group is the same as in **Figure 3**. Each scatterplot shows the summation of C-FOS distributional differences along the AP axis (sum of ΔC-FOS) versus the significance (Adjusted *P* value) for each brain

1278 region of the pairwise-compared groups. Statistical analysis is the same as described in **Figure**
1279 **3**. Vertical and horizontal dotted lines represent the sum of ΔC-FOS = 0 and Adjusted *P* value
1280 = 0.05, respectively. Brain region color codes are as described in **Figure 3**. Open and filled
1281 circles represent ROI-non-corrected and -corrected brain regions, respectively.

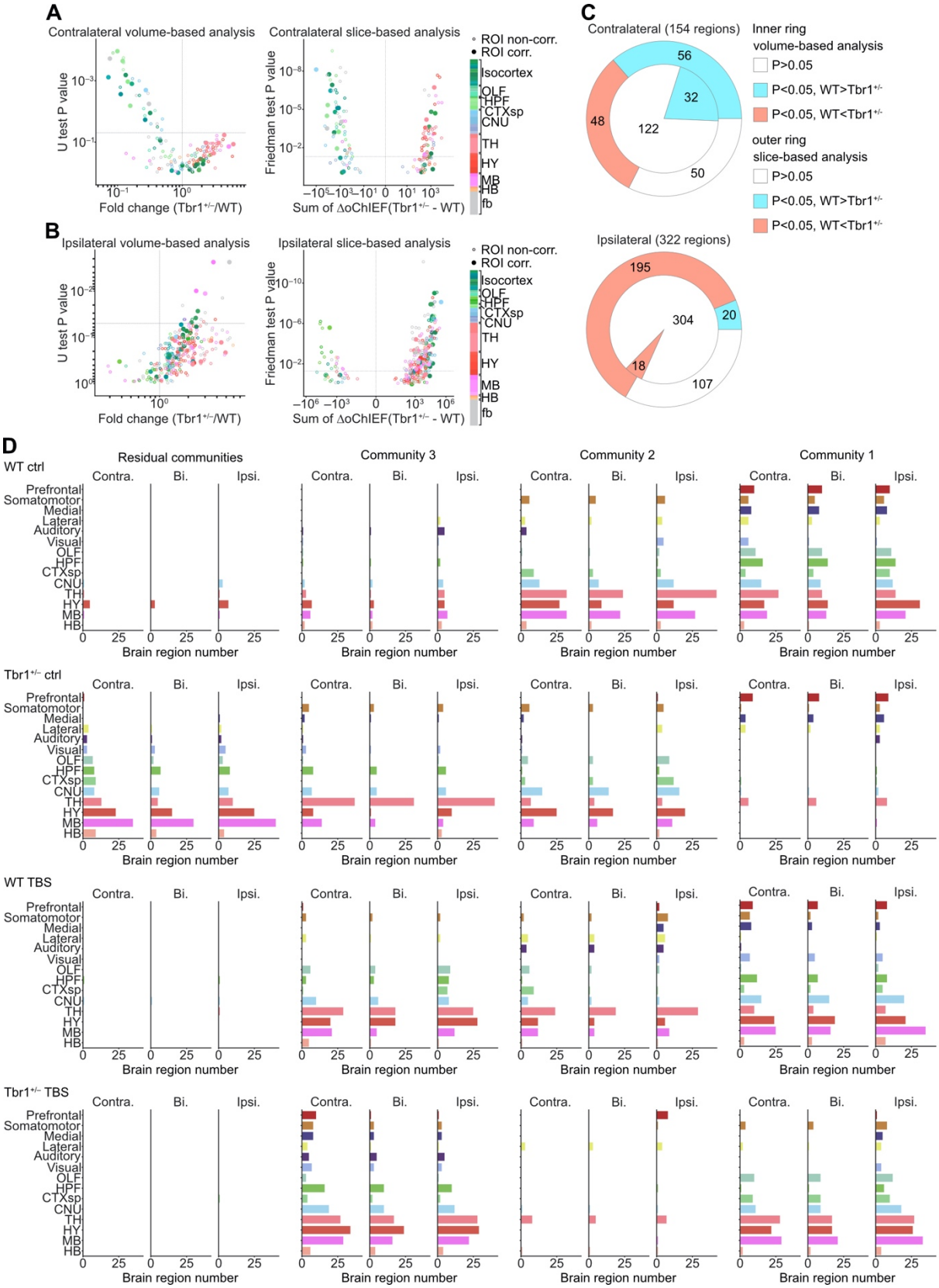

Figure S7. Comparison of volume-based and slice-based analysis of binarized oChIEF signals and summary of the region compositions in the communities of activity correlation networks.

1286 (A)-(B) Binarized oChIEF percentages (volume-based analysis) versus oChIEF pixel
1287 distributions along the AP axis (slice-based analysis) used for structure-wise comparisons
1288 between the contralateral (A) and ipsilateral (B) hemispheres of wild-type and *Tbr1*$^{+/-}$ mouse
1289 brains. The dataset and plots in the volume-based analysis are similar to those in **Figure 2C**
1290 except the compared regions represent a subset from the **Figure 2C** dataset to facilitate
1291 comparison with the slice-based analysis. Thus, the brain regions compared in this figure are
1292 identical for both volume-based and slice-based analyses. Statistical analysis of volume-based
1293 quantification was performed as described in **Figure 2C**. Scatterplots of slice-based analysis
1294 showing the summation of oChIEF difference along the AP axis (sum of ΔoChIEF) versus
1295 significance (Friedman test *P* value, determined by Friedman one-way repeated measure
1296 analysis) for each brain region. Vertical and horizontal dotted lines represent the sum of
1297 ΔoChIEF = 0 and Friedman test *P* value = 0.05, respectively. Brain region color codes are as
1298 described in **Figure 2C**. Open and filled circles represent ROI-non-corrected and -corrected
1299 brain regions, respectively. Sample sizes of mice in (A) and (B) are identical to those described
1300 in **Figures 2** and **4**, respectively.
1301 (C) Pie charts summarizing the differences in structure-wise comparisons between the volume-
1302 based and slice-based analyses shown in (A) and (B).
1303 (D) The various plots represent different communities (rows) in different networks (columns).
1304 The plots show the numbers of brain regions involved in different brain areas. The data for
1305 the contralateral and ipsilateral brain hemispheres are presented separately, with numbers of
1306 bilaterally involved brain regions also indicated.
1307

1308 **Supporting Tables and Videos**

1309

1310 **Table S1** Results for oChIEF-Citrine and C-FOS signals using volume-based analyses.

1311 **Table S2** Results for oChIEF-Citrine and C-FOS signals using slice-based analyses.

1312 **Table S3** Network analysis based on C-FOS expression.

1313 **Video S1** Coronal brain slice series of binarized oChIEF signals (green) superimposed on a

1314 CCFv3 template (gray). Wild-type (WT), upper; *Tbr1*$^{+/-}$, lower.

1315 **Video S2** Summarized 3D stacks with binarized and binned (10 μm^3) oChIEF signals from 13

1316 WT (upper) and 15 *Tbr1*$^{+/-}$ (lower) mouse brains.

1317
1318